

Nowcasting Storm Initiation and Growth Using *GOES-8* and *WSR-88D* Data

RITA D. ROBERTS

Research Applications Program, National Center for Atmospheric Research, Boulder, Colorado

STEVEN RUTLEDGE

Department of Atmospheric Sciences, Colorado State University, Fort Collins, Colorado

(Manuscript received 14 January 2002, in final form 4 November 2002)

ABSTRACT

The evolution of cumulus clouds over a variety of radar-detected, boundary layer convergence features in eastern Colorado has been examined using Geostationary Operational Environmental Satellite (*GOES*) imagery and Weather Surveillance Radar-1988 Doppler (*WSR-88D*) data. While convective storms formed above horizontal rolls in the absence of any additional surface forcing, the most intense storms initiated in regions above: gust fronts, gust front interaction with horizontal rolls, and terrain-induced stationary convergence zones. The onset of vigorous cloud growth leading to storm development was characterized by cloud tops that reached subfreezing temperatures and exhibited large cooling rates at cloud top 15 min prior to the first detection of 10-dBZ radar echoes aloft and 30 min before 35 dBZ. The rate of cloud-top temperature change was found to be important for discriminating between weakly precipitating storms (<35 dBZ) and vigorous convective storms (>35 dBZ). Results from this study have been used to increase the lead time of thunderstorm initiation nowcasts with the NCAR automated, convective storm nowcasting system. This improvement is demonstrated at two operational forecast offices in Virginia and New Mexico.

1. Introduction

This study shows how Geostationary Operational Environmental Satellite (*GOES*) imagery and Weather Surveillance Radar-1988 Doppler (*WSR-88D*) data can be used by a forecaster to monitor the development of cumulus clouds into vigorous convective storms and how this process of monitoring cloud growth can be automated to produce additional lead time on convective storm nowcasting. Vigorous convective storms are defined here as precipitating cumulus congestus and cumulonimbus clouds containing radar reflectivities greater than 35 dBZ. Satellite and radar data are combined explicitly for the purpose of documenting precursor information on the initiation, growth, and intensification of convective storms. Automated detection of precursor information is incorporated into the National Center for Atmospheric Research (NCAR) convective storm nowcasting system (Mueller et al. 2000; Mueller et al. 2003) to extend the lead time in issuing time- and place-specific nowcasts of convective storm initiation. Nowcasts here refer to short-term 0–1-h forecasts. It will be shown for the cases presented that automated 30-min nowcasts

have increased accuracy and lead time over nowcasts produced using radar information alone.

Numerous studies using satellite, radar, and mesonet data have documented the importance of convergence boundaries within the convective boundary layer (CBL) in the initiation of new convection or enhancement of existing convection (Byers and Braham 1949; Pielke 1974; Purdom 1976; Holle and Maier 1980; Wade and Foote 1982; Purdom and Marcus 1982; Wilson and Schreiber 1986; Wilson et al. 1992; Wilson and Mueller 1993; Fankhauser et al. 1995; Weckwerth et al. 1996; among others). One of the earliest operational detections of a sea-breeze front and thunderstorm outflow was made using a Weather Surveillance Radar-1957 (*WSR-57*; Boyd 1965). The radar finelines associated with these two features were observed on radar to collide, and several building cumuli were subsequently observed visually in the direction of the colliding boundaries. A decade later, Purdom (1976) demonstrated how *GOES* satellite imagery provided valuable information on the initiation and maintenance of convective activity, by its ability to detect enhancement of convective cloudiness along a sea-breeze front prior to thunderstorm development. Wilson and Carbone (1984) and Wilson and Schreiber (1986) have shown that a forecaster could track and monitor convergence boundaries using single-Doppler radar for the purpose of forecasting thunder-

Corresponding author address: Dr. Rita D. Roberts, NCAR/Research Applications Program, P.O. Box 3000, Boulder, CO 80307-3000.
E-mail: rroberts@ucar.edu

storm initiation, even when clouds were absent above the boundaries. However, monitoring surface convergence boundaries alone does not provide specific information on the timing and location of convection (Stensrud and Maddox 1988; Wilson and Mueller 1993). Provided the atmosphere is at least conditionally unstable, thunderstorms often form in the vicinity of these boundaries. The challenge in nowcasting convection arises in knowing if there is sufficient instability in the vicinity of a surface convergence feature for vigorous convection. In addition, there is the uncertainty in knowing if the amount of boundary layer moisture measured by the most recent National Weather Service (NWS) rawinsonde is representative of the available moisture in regions located some distance from where the sounding was taken and, thus, representative of the amount of atmospheric instability present there (Mueller et al. 1993; Weckwerth et al. 1996).

Until the variability in static stability and moisture can be measured operationally with high spatial resolution over a large domain, satellite data are the only operationally available dataset that provides an indirect measure of stability; that is, sufficient moisture and instability exist for lifted parcels to reach the lifting condensation level. Several studies have used satellite data in conjunction with research radar, aircraft, and photogrammetric techniques to examine the location of cumulus clouds relative to boundary layer horizontal rolls (LeMone 1973; Weckwerth et al. 1997), sea-breeze fronts (Wakimoto and Atkins 1994; Atkins et al. 1995), and drylines (Atkins et al. 1998). In this study the *GOES-8* and WSR-88D data, operationally available every 15 and 6 min (in storm mode), respectively, can now be used to document cumulus cloud development above boundary layer convergence features. This is possible in part because of the smaller errors (<4 km) in registration of the *GOES-8* satellite data (compared to >4 km errors for *GOES-7*) enabling more accurate cumulus cloud locations. With the improved spatial and temporal resolution of the *GOES* satellites (see Menzel and Purdom 1994), it is now possible to track the evolution of cumulus cloud development—approaching the cumulus timescale—by monitoring the cloud-top infrared brightness temperatures. Operational WSR-88Ds are sensitive enough to detect not only the velocity and reflectivity features associated with surface convergence boundaries, but also first radar echoes at close range (echoes with reflectivities of -10 to 5 dBZ).

Much attention has been directed at combining satellite and radar information for forecasting precipitation rate and thunderstorm intensity (Griffith et al. 1978; Reynolds and Smith 1979; Lovejoy and Austin 1979; Negri and Adler 1981; Browning and Collier 1982; Collier and Lilley 1994; Hand 1996; Pierce et al. 2000) and toward building automated thunderstorm forecasting systems (Dixon and Wiener 1993; Hand and Conway 1995; Hand 1996; Golding 1998; Pierce et al. 2000). Each of the latter systems or techniques depends on

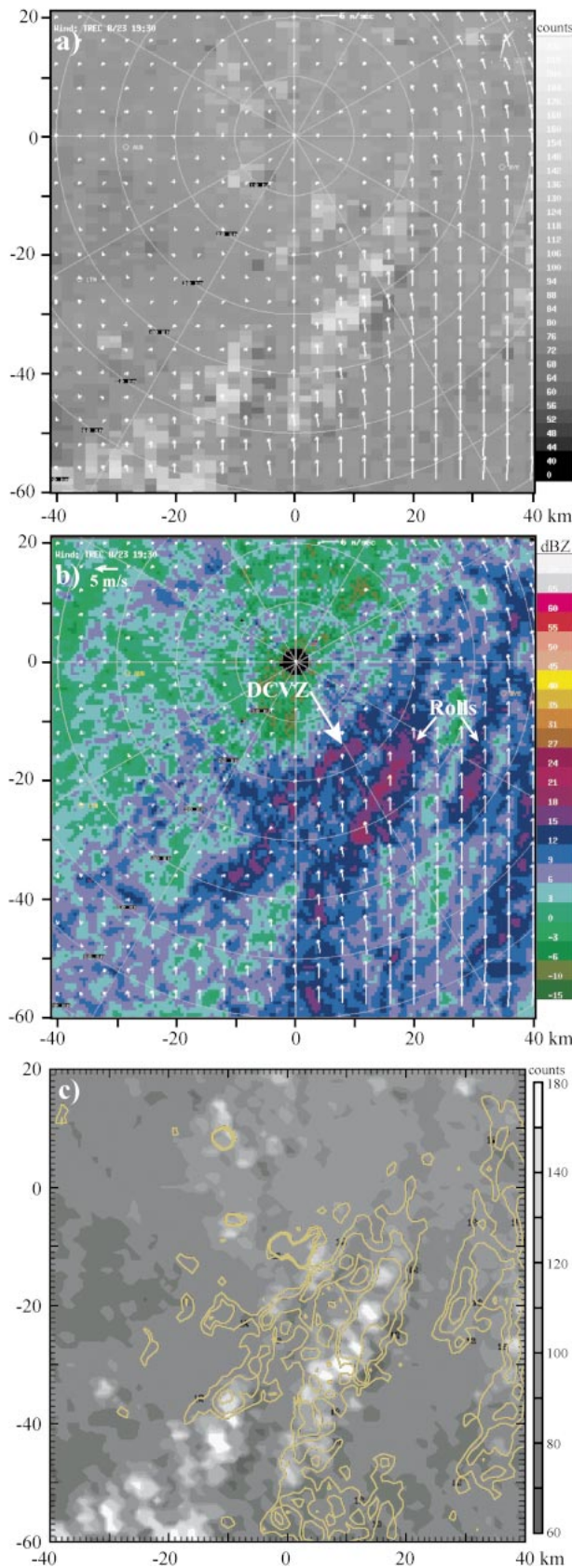
tracking existing storms, and does not explicitly address the initiation of new thunderstorms using satellite and boundary layer radar features. Mueller et al. (2003) document a convective storm nowcasting system (Auto-Nowcast System, referenced here as the ANC system) that relies heavily on radar detection and tracking of convergence boundaries as the first step in forecasting thunderstorm initiation. The ANC system incorporates satellite information for nowcasting thunderstorm initiation based on results of this study.

A description of data processing is provided in section 2. In section 3 we present a case that demonstrates the concept for monitoring the growth of clouds into convective storms and test this concept on additional days in which the boundary layer convergence features varied. We then show in section 4 the methodology for incorporating this application into the ANC system and its operational performance at two different forecast offices. A few summary comments are provided in section 5.

2. Data processing

The primary radar data used in this study are the Archive Level II data collected by the Denver WSR-88D S-band (10 cm wavelength) radar located approximately 20 km to the southeast of the Denver International Airport (DIA) and 60 km to the east of the Colorado Front Range. Level II data from the Sterling, Virginia, and White Sands, New Mexico, WSR-88Ds are also utilized. While the WSR-88D actually transmits and receives pulse volumes having gate spacing of 250 m, Level II data are only archived at 1-km reflectivity and 250-m radial velocity gate spacing. For the cases shown in this study, the radar scanned in precipitation mode Volume Coverage Pattern (VCP) 21, which is a 6-min scan composed of nine 360° surveillance sweeps ranging from 0.5° to 19.5° in elevation [OFCM (1991); *Federal Meteorological Handbook No. 11* (FMH-11)]. WSR-88Ds use bypass filter maps for removal of ground clutter (FMH-11). For this reason, no editing for clutter removal was performed. Thresholding on reflectivity is also done on the radar data prior to Level II archival in regions where the signal-to-noise ratio was less than 5 dB (usually about 3 dB; FMH-11). Signals lower than about -15 dBZ at close range and -5 dBZ at longer ranges are removed by the radar processor because their intensity is not 3 dB above the noise level. The sensitivity of the radar to pick up these weak signals is important, especially for detecting Bragg scatter echo along the perimeter of cumulus clouds (Knight and Miller 1993) and detecting clear air return due to insects (Wilson et al. 1994).

The *GOES-8* visible ($0.62 \mu\text{m}$; channel 1) and infrared ($10.7 \mu\text{m}$; channel 4) imager data at 15-min intervals are used in this study. The *GOES-8* visible channel has improved imager resolution over *GOES-7* and improved signal to noise in the IR channels making it capable of resolving finer detail than its predecessors (Menzel and



Purdom 1994). The data are processed at 1.0-km resolution for the visible (VIS) and 4.0-km resolution for the IR. Parallax is a significant problem when viewing clouds at locations of increasing satellite nadir angles. Weiss (1978) and Rao et al. (1990) illustrate how the apparent cloud location can be significantly displaced from the actual cloud location. In eastern Colorado, at a nadir angle of 40° , there is approximately a 1 to 1 correspondence in magnitude between the height of a cloud and its horizontal displacement on an image due to the parallax view (Johnson et al. 1994). In order to compare datasets the radar data were interpolated to a rectangular Cartesian grid and the native satellite data were projected onto an Albert equal-area (Synder 1983), conformal Cartesian grid and adjusted to correct for parallax viewing angle at each location.

3. Growth of cumulus clouds

In this section we document the growth of clouds in the vicinity of a variety of surface convergence features within the CBL. Surface convergence boundaries examined here include thunderstorm outflows, wind shift lines, colliding gust fronts, horizontal boundary layer rolls, terrain-induced convergence zones, and the intersection of horizontal rolls with gust fronts. The data were collected over northeastern Colorado in 1995. Summertime convection in this area is often initiated by boundary layer forcing in the form of convergence boundaries in conditionally unstable environments (Wilson and Schreiber 1986; Wilson and Mueller 1993; Mueller et al. 1993) with more intense thunderstorms resulting from a combination of boundary layer and weak synoptic-scale forcing (Doswell 1980; Szoke et al. 1984; Roberts and Wilson 1995). Although Dye et al. (1989) and Gremillion and Orville (1999), among others, have shown that onset of storm electrification generally occurs >5 min after storm echoes of 30 dBZ or greater have reached subfreezing levels, we do not refer to the storms herein as thunderstorms, nor do we attempt to correlate radar and satellite-based signatures in our cases to the onset of lightning.

a. Signatures in satellite and radar imagery

1) VISIBLE SATELLITE AND CLEAR-AIR RADAR REFLECTIVITY

On 23 August 1995 a few lines of cumulus clouds were present in the satellite imagery in the early af-

←

FIG. 1. Comparison of GOES satellite and Denver, CO, WSR-88D radar data on 23 Aug 1995 at 2228 UTC. (a) Visible imagery (in counts; 256 is equivalent to 100% albedo), (b) radar reflectivity at 0.5 km AGL. TREC cross-correlation vectors (see text) are overlaid onto (a) and (b). (c) Cartesian plot of visible imagery (in counts) with contours of reflectivity overlaid. Contours are in increments of 12, 14, and 16 dBZ.

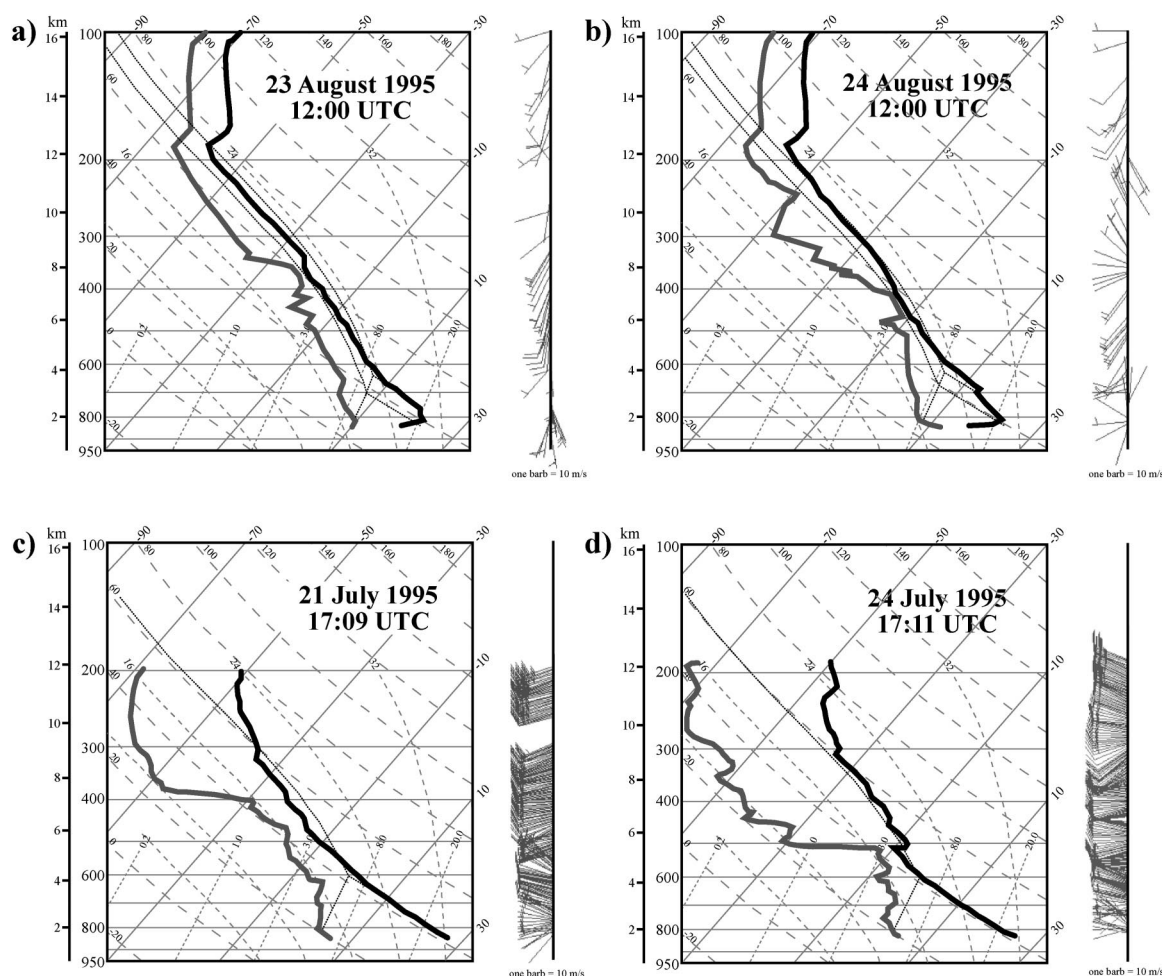


FIG. 2. Rawinsonde plots from Denver. The height scale corresponding to the pressure levels is in km MSL. (a) NWS sounding at 1200 UTC 23 Aug 1995, (b) NWS sounding at 1200 UTC 24 Aug 1995, (c) special sounding taken at 1709 UTC 21 Jul 1995, and (d) special sounding taken at 1711 UTC 24 Jul 1995.

ternoon; two are shown in Fig. 1a at 1928 UTC (all times listed are in UTC; subtract 6 h for local time). At the same time, the radar reflectivity data (Fig. 1b) show the presence of two distinct CBL convergence features: 1) N-S-oriented horizontal convective rolls indicated on radar at 0.5 km AGL as linear, reflectivity thin lines spaced here approximately 8 km apart and 2) the presence of a semistationary Denver convergence vorticity zone (DCVZ), a terrain-induced region of convergence between moist south-southeasterly flow over the plains with northwesterly drier flow off the Rocky Mountains to the west (Szoke et al. 1984; Crook et al. 1990). The DCVZ is reflected in the boundary layer winds, obtained using a cross-correlation echo tracker (TREC; Tuttle and Foote 1990), that are overlaid in Figs. 1a and 1b where the stronger southerly flow converges with the weaker north-northwesterly flow. No storm echoes are present at this time. Combining the reflectivity information with the cloud imagery (Fig. 1c) shows the cumulus cloud lines are

associated with the DCVZ and particularly with the more western horizontal roll. The correlation of the cumulus cloud lines with the radar-detected DCVZ and horizontal rolls is especially significant for two reasons. First, no adjustment had to be made to the satellite data to correct for registration errors, which was often a problem with GOES satellites prior to 1995. Second, it demonstrates that satellite information can be directly linked to boundary layer, radar features with the potential for both datasets to be used together quantitatively to address the changing CBL and its impact on cloud growth.

By 2130 UTC, the convective temperature was achieved and the small amount of convective inhibition (CIN) in the sounding (Fig. 2a) was overcome. Storms were well established along the SW portion of the DCVZ and new storms were forming at the intersections of the horizontal rolls with the DCVZ, a favorable location for new storm development (Wilson et al. 1992; Atkins et al. 1995; Atkins et al. 1998) due to the in-

tensification of convergence at those points. Also at this time, the number of horizontal rolls had decreased and they were spaced >10 km apart, indicating that the depth of the CBL had increased (Weckwerth et al. 1997). Cumulus cloud lines with highest cloud albedos found at the intersection points were present in the visible imagery (not shown).

2) INFRARED BRIGHTNESS TEMPERATURES AND BRAGG SCATTER ECHO

To examine the pattern of cloud growth above the convergence lines shown in Fig. 1, infrared brightness temperatures, visible imagery, and radar reflectivities at 4.5 km AGL are compared at 15-min intervals from 1930 to 2030 UTC (Figs. 3 and 4). The 4.5-km level was chosen as it is the height at which many of the first radar precipitation echoes are detected in this case. For Denver, this is equivalent to 6.1 km MSL on the NWS soundings. Initially, the cloud lines (Figs. 3a,d) are composed primarily of cumulus clouds. Cloud-top temperatures (Fig. 3b) are generally cooler (ranging from 0° to 20°C) compared to the clear-sky background temperatures of 30° – 40°C (light green/orange colors). At 1945 UTC (Fig. 3e), cloud-top temperatures remain warmer than freezing except above the SW edge of the DCVZ at location ($x = -25$, $y = -54$) where temperatures have now dropped below 0°C . Maximum reflectivities are <0 dBZ during this 15-min period (Figs. 3c,f) indicating precipitation formation has not yet begun; that is, cold-cloud ice nucleation processes have not yet produced hydrometeors (ice crystals, snow, graupel) detectable by the S-band radar. Knight and Miller (1993) in their study of cumulus clouds have shown that reflectivities in the range of -10 to $+5$ dBZ from a 10-cm radar are caused by Bragg scattering, that is, back scattering by refractive index gradients along the peripheries of cumulus clouds. They found that reflectivities >5 dBZ are due to Rayleigh scattering from precipitation particles. In this study, reflectivities >5 dBZ will be defined as precipitation echoes.

The ring of weak echo surrounding the radar is an artifact resulting from the technique used to interpolate the radar data to a Cartesian grid causing clear-air radar return from the boundary layer to be interpolated upward at higher altitudes. The weak -15 to 0 dBZ “clear air” reflectivity return located along the cloud line is likely attributable to both backscattered energy return from insects (Wilson et al. 1994; Christian and Wakimoto 1989) caught up in the updrafts of the horizontal convective rolls and Bragg scattering from the cumulus clouds.

Over the next 30 min, there is noticeable growth of the cloud lines as evidenced by the increased areal extent and albedo of the clouds (Figs. 4a,d,g) and $\sim 10^{\circ}\text{C}$ temperature decreases at each successive time period (Figs. 4b,e,h) as the cloud tops extend to higher heights and colder subfreezing temperatures. A distinct change in

the radar signatures has also occurred. From 2000 to 2015 UTC, the cumulus clouds located above the intersection point of the DCVZ with a horizontal roll now have a continuous region of -10 to 0 dBZ echo associated with it. Cloud growth in the SW portion of the cloud line has produced echo that has intensified from <5 dBZ to reflectivities of >35 dBZ, a precipitating echo. These expanded regions of echo return are only evident above 3.5 km AGL during this period, 1.5 km above the level of free convection (see Fig. 2a). Clear-air, boundary layer reflectivity signatures now extend only to 2.5 km at 2000 UTC, except in the circular artifact area surrounding the radar. With cloud-top temperatures now close to freezing, the -10 to 5 dBZ echoes along the line (Figs. 4c,f) at 4.5 km are predominantly caused by Bragg scattering from the edges of the growing cluster of cumulus clouds. By 2030 UTC, extensive growth of the clouds has occurred (Fig. 4g) and in those areas where cloud-top temperatures have fallen well below freezing (blue areas, Fig. 4h), precipitation echoes are now detected by radar (Fig. 4i). These clouds quickly evolved into large storms.

3) TRENDS ASSOCIATED WITH THE SEMISTATIONARY CONVERGENT LINE

The information presented in Fig. 4 suggests that the satellite sensing of cloud-top cooling that precedes the detection of storms on radar could be used as a precursor signature for convective storm initiation. The significance of freezing cloud-top temperatures in relation to precipitation formation in the storms can be readily seen in the time series plot shown in Fig. 5. The implication is that once clouds grow to a height where they radiate at subfreezing temperatures (satellite radiometers sense radiation only to a depth of ~ 200 – 500 m within a cloud) the ice nucleation process is initiated near the tops and first echo precipitation, likely in the form of graupel, results (Dye and Martner 1982). Knight et al. (1983) document results of a comparison of cloud photography with high-resolution, research radar observations of first (5 dBZ) echo in eastern Colorado cumulus clouds. They found in general that first radar echo typically appeared near or at visual cloud top and extended over the depth of the visible cloud 0–11 min after cloud tops reached environmental temperatures between -15° and -20°C . Because their study lacked visual data early in the cloud(s) lifetime (i.e., at temperatures warmer than -10°C), they suggested that a more conservative estimate is a time interval of 15 min from the tops passing the -10°C level to the first echo occurrence (5 dBZ). Comparatively, the clouds in Fig. 5 are developing much faster, reaching 5 dBZ 15 min from the tops passing the 0°C level, and 35 dBZ by the time cloud tops have reached -10°C . The corresponding environmental temperature from the sounding at the height of this cloud is -15°C , 5°C cooler than the cloud parcels. Time series

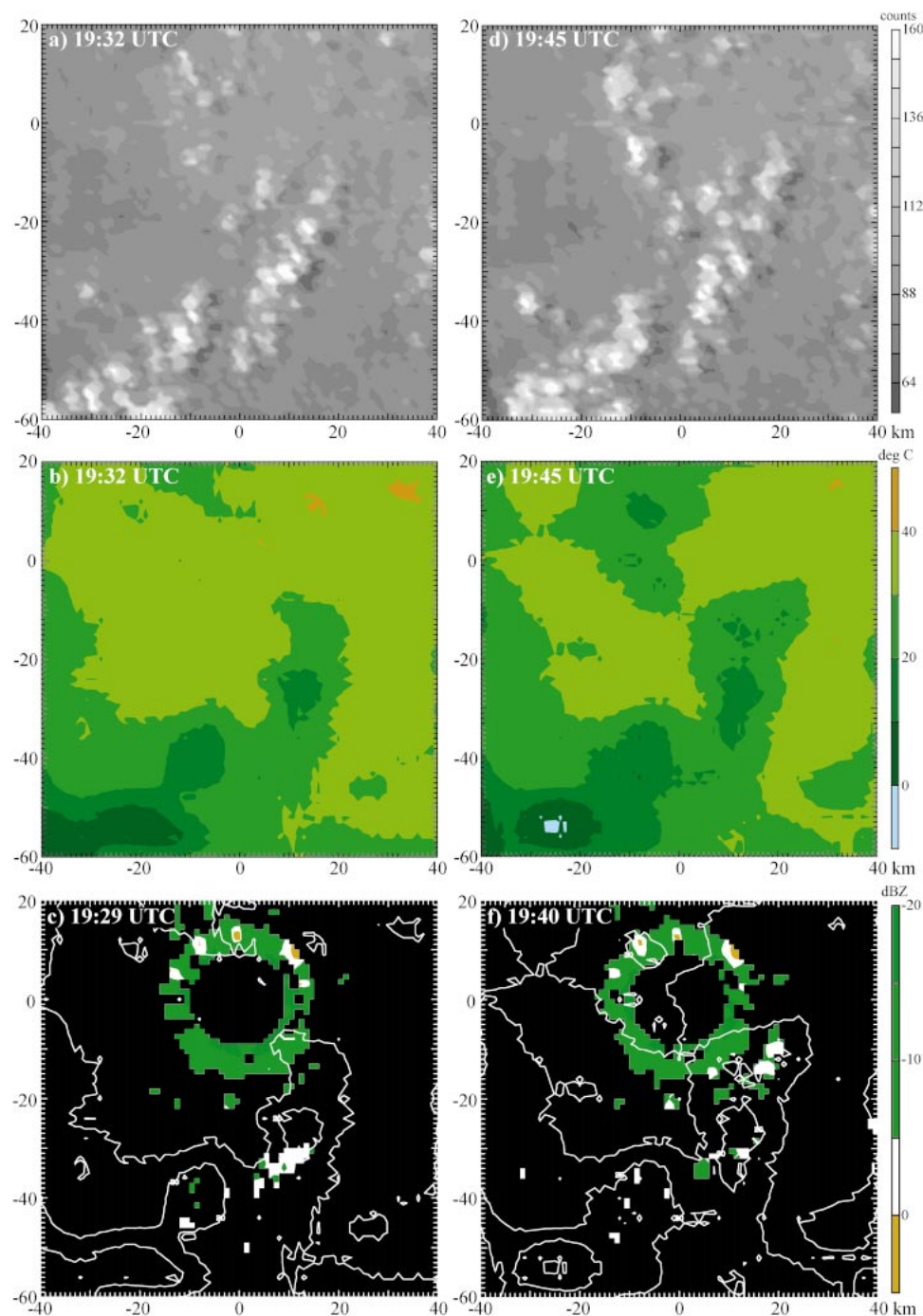


FIG. 3. Cartesian plots of satellite visible imagery (counts), infrared brightness temperatures ($^{\circ}\text{C}$), and Denver radar reflectivity (dBZ) data at 4.5 km AGL on 23 Aug 1995. (a) Visible imagery at 1932 UTC, (b) IR temperatures at 1932 UTC, (c) reflectivity at 1929 UTC with contours of IR brightness temperatures from (b) overlaid, (d) visible imagery at 1945 UTC, (e) IR temperatures at 1945 UTC and (f) reflectivity at 1940 UTC with contours of IR brightness temperatures from (e) overlaid. The ring of echo in (c) and (f) is an artifact generated by the Cartesian process (see text).

plots from other cases presented in section 3 agree more closely with the Knight et al. results.

It is important when nowcasting storm initiation to not only monitor cloud-top temperatures, but also to

monitor the rate of change (hereafter referred to as ROC) of the brightness temperatures. For two 15-min intervals shown in Fig. 6, the temperature ROC shifts to greater temperature falls as the clouds undergo growth. The

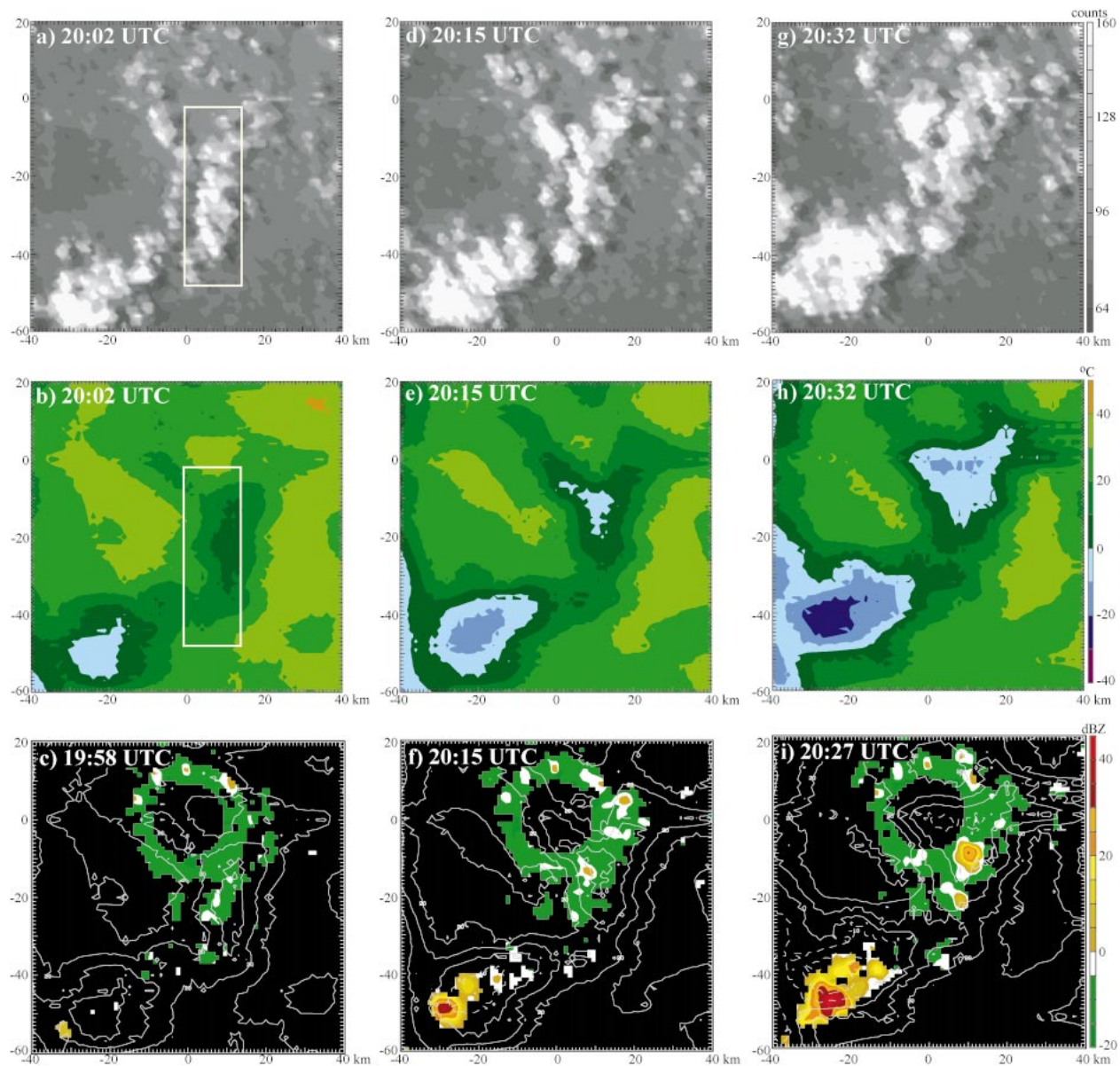


FIG. 4. Same as in Fig. 3 except at time periods 2002, 2015, and 2032 UTC, approximately, on 23 Aug 1995. The boxes in (a) and (b) define the domain used for monitoring the cloud growth trends shown in Fig. 5.

median ROC values reflect this best, evolving from -3°C in 15 min in Fig. 6a to -8°C in 15 min in Fig. 6b. The median ROC values for all 15-min time intervals are listed below the temperature curve in Fig. 5. The largest negative values correspond to the periods of intense cloud growth. It is worth noting that the rate values correlate well with the rate of moist-adiabatic expansion between 5.0 and 8.1 MSL (Fig. 2a). The ROC information can be very helpful in distinguishing between active and suppressed growth of clouds, as will be shown later. It is possible that regular comparison of cloud-top temperatures to the sounding temperatures at equivalent heights could be useful for identifying vig-

orous cloud growth if cloud-top parcels are much warmer than the environment, but we do not specifically address this in this study.

Most storm tracking algorithms used in nowcasting systems to predict future storm locations typically do not identify and track echoes until they reach 30–35 dBZ [e.g., the Thunderstorm Identification, Tracking, Analysis and Nowcasting algorithm (TITAN; Dixon and Wiener 1993) and the Storm Cell Identification and Tracking algorithm (SCIT; Johnson et al. 1998)]. By monitoring cloud-top temperatures when they first drop below 0°C and detecting large rates of temperature change, extra lead time can be gained in nowcasting

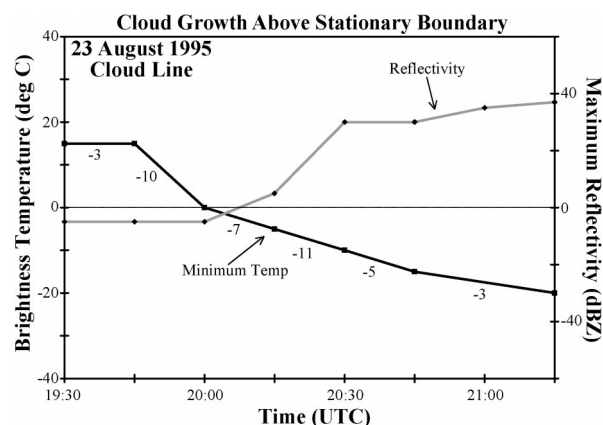


FIG. 5. Time series plot of minimum IR brightness temperature (black curve) in $^{\circ}\text{C}$ and maximum radar reflectivity (gray curve) in dBZ associated with growth of the cloud line (shown in Figs. 4a,b) above the semistationary DCVZ on 23 Aug. ROC values determined over 15-min intervals from histogram data (as illustrated in Fig. 6) are listed below the temperature curve.

storm initiation. *Here the satellite data give information on vigorous cloud development ~30 min in advance of significant radar echoes.* The representativeness of this particular finding and its operational utility are addressed in section 3b.

b. Growth above a variety of convergence boundaries

In this section, data from three additional days are presented to illustrate how the change in brightness temperature is related to storm initiation and growth in three different boundary layer scenarios. To nowcast the specific *time and location* of new storms, it is necessary to track cloud-top temperature tendencies over domains smaller than the length of a cloud line since a variety of factors can influence which clouds, if any, along the line will grow into storms. Thus, time series plots are now obtained by monitoring the data over 20-km-square windows—a smaller domain size yet large enough to account for any cloud and boundary motion during the 4-h time period of afternoon convection. Cloud-top temperature plotted during the early periods of the time series data represent temperatures originating from more than one cumulus cloud, that is, the minimum temperature from a cluster of cumulus clouds that fills some portion of the 20-km square box. The minimum temperature and maximum reflectivity within the box are plotted in the time series figures shown in the next sections.

1) GROWTH ASSOCIATED WITH GUST FRONT PASSAGE

The atmosphere on 24 August 1995 was conditionally unstable (Fig. 2b). Although storms developed early over the Rocky Mountains at 2000 UTC (see western portion of visible satellite image in Fig. 7a)

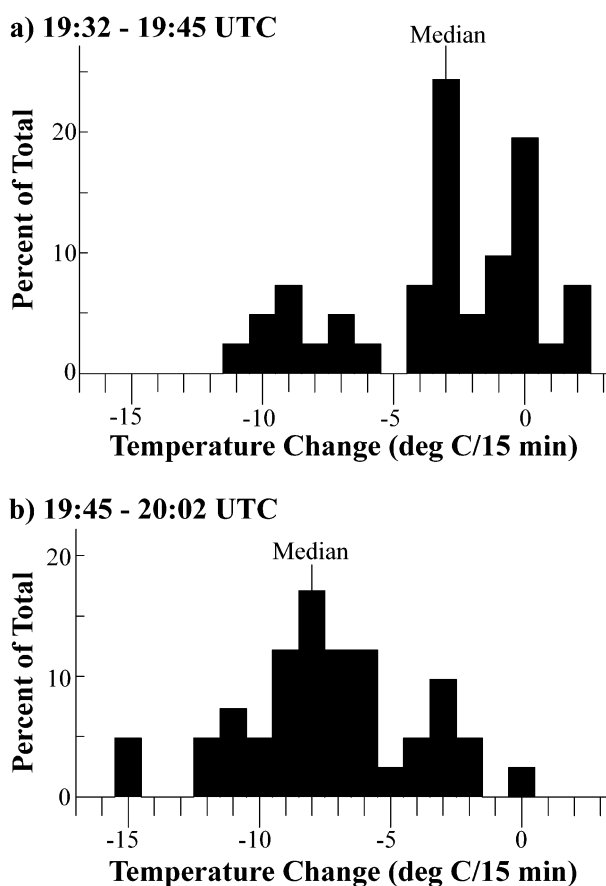


FIG. 6. Histogram plots of change in brightness temperature with time on 23 Aug within the boxed domains shown in Figs. 4a,b for the time periods (a) 1932–1945 UTC and (b) 1945–2002 UTC. The thin vertical line above the histogram bars is the median value within the boxed domain.

and the convective temperature east of the Rockies was reached an hour later at 2100 UTC based on surface mesonet data, some boundary layer forcing was still required to trigger convection over the northeastern plains. The CBL convergence features present during the afternoon included two gust fronts, horizontal rolls, and gust front interaction with horizontal rolls. Some of these features can be seen in the low-level radar reflectivity field at 2230 UTC (Fig. 7b). The NE–SW linear features are horizontal convective rolls which appear on radar as clear-air reflectivity thin lines oriented parallel to the low-level wind field (Christian and Wakimoto 1989). Clusters of cumulus clouds were present over the plains at 2000 UTC (see Fig. 7a) with only a slight suggestion that they have some linear orientation parallel to the NE–SW-oriented horizontal rolls, but nothing as obvious as seen with the 23 August case (Figs. 3 and 4). At 2230 UTC, it would be difficult to say from the radar image alone, Fig. 7b, exactly where the new storms are going to form in the next 30 min associated with these bound-

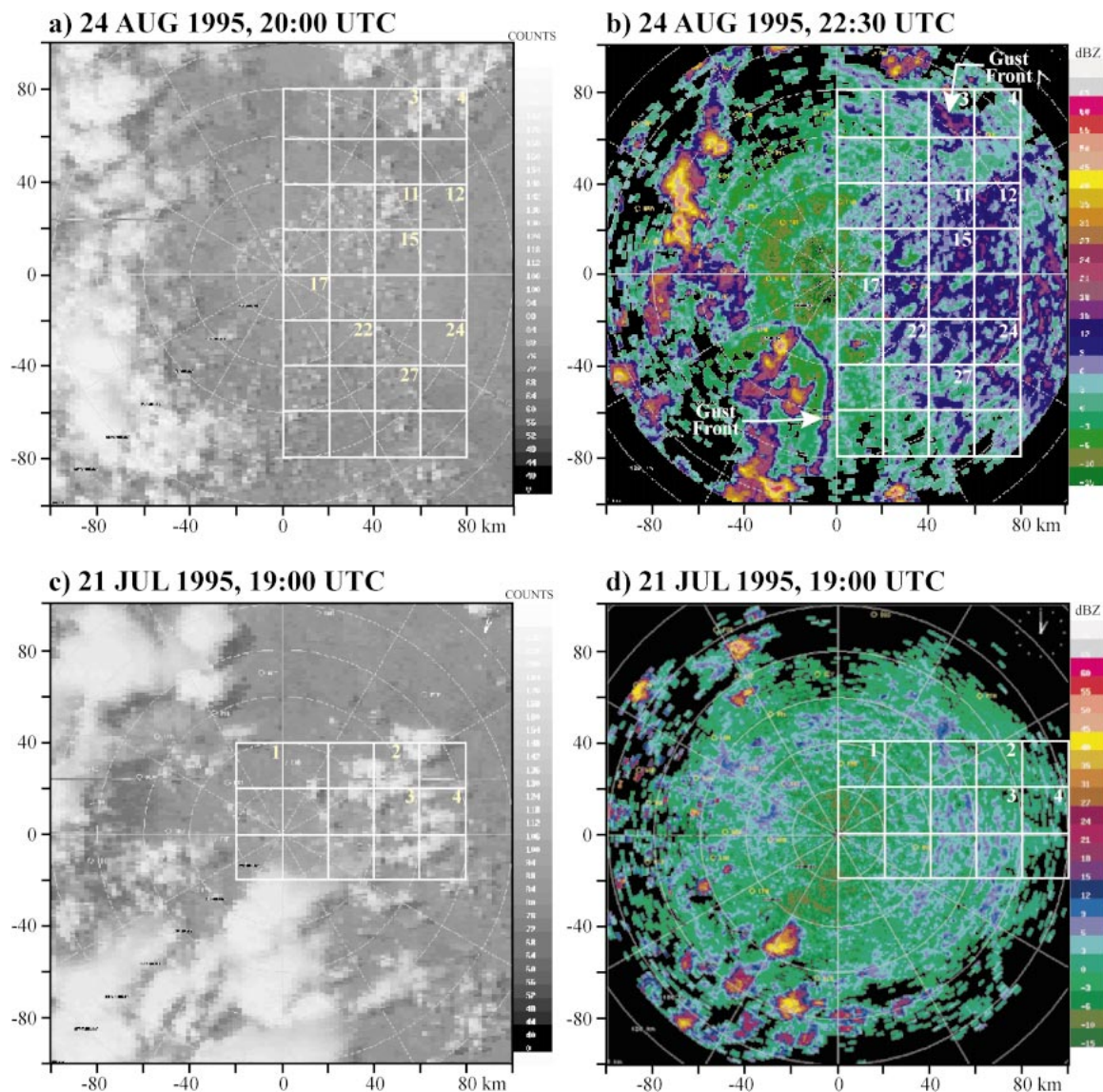


FIG. 7. Visible satellite imagery and radar reflectivity data at 0.5 km AGL for two different days. (a) Visible imagery at 2000 UTC 24 Aug 1995. Units are radiance counts (256 counts is equivalent to 100% albedo). (b) Radar reflectivity at 2230 UTC 24 Aug. (c) Visible imagery (counts) at 1900 UTC 21 Jul 1995 and (d) radar reflectivity (dBZ) at 1900 UTC 21 Jul. The gridded overlays represent 20 km \times 20 km domains used to analyze trends in growth during the afternoon.

ary layer features. Numbered boxes in Fig. 7 have been selected to illustrate patterns of cloud growth.

Time series data for boxes 3 and 4 are shown in Figs. 8a and 8b, respectively. A gust front from the north enters these domains at 2230 UTC (Fig. 7b). Ahead of this gust front, during the period prior to 2230 UTC (Figs. 8a and 8b), some cloud growth has occurred as cloud tops reach subfreezing temperatures and weak precipitation storms are detected on radar (<30 dBZ). These storms do not persist for long and in both boxed areas these storms actually begin to dissipate, as evidenced by the decrease in maximum reflectivities, warming of cloud-top temperatures, and positive rates of temperature change ahead of the gust front. With the

passage of the gust front, clouds grow to much higher heights as indicated by the $<-40^{\circ}\text{C}$ temperatures and the more intense reflectivity storms that occur after 2230 UTC (Figs. 8a and 8b).

It can be seen in Fig. 8 that there are differences in the growth rates and intensification of individual storms along the boundary. Other factors, not discussed in this study, have an impact on the rate at which these storms grow. These include 1) the magnitude and orientation of the low-level shear relative to the boundary; 2) the prevailing steering winds; 3) the stability of the atmosphere; 4) the strength of convergence and vertical motion along a boundary; 5) the movement of clouds relative to the boundary layer convergence, that is, the

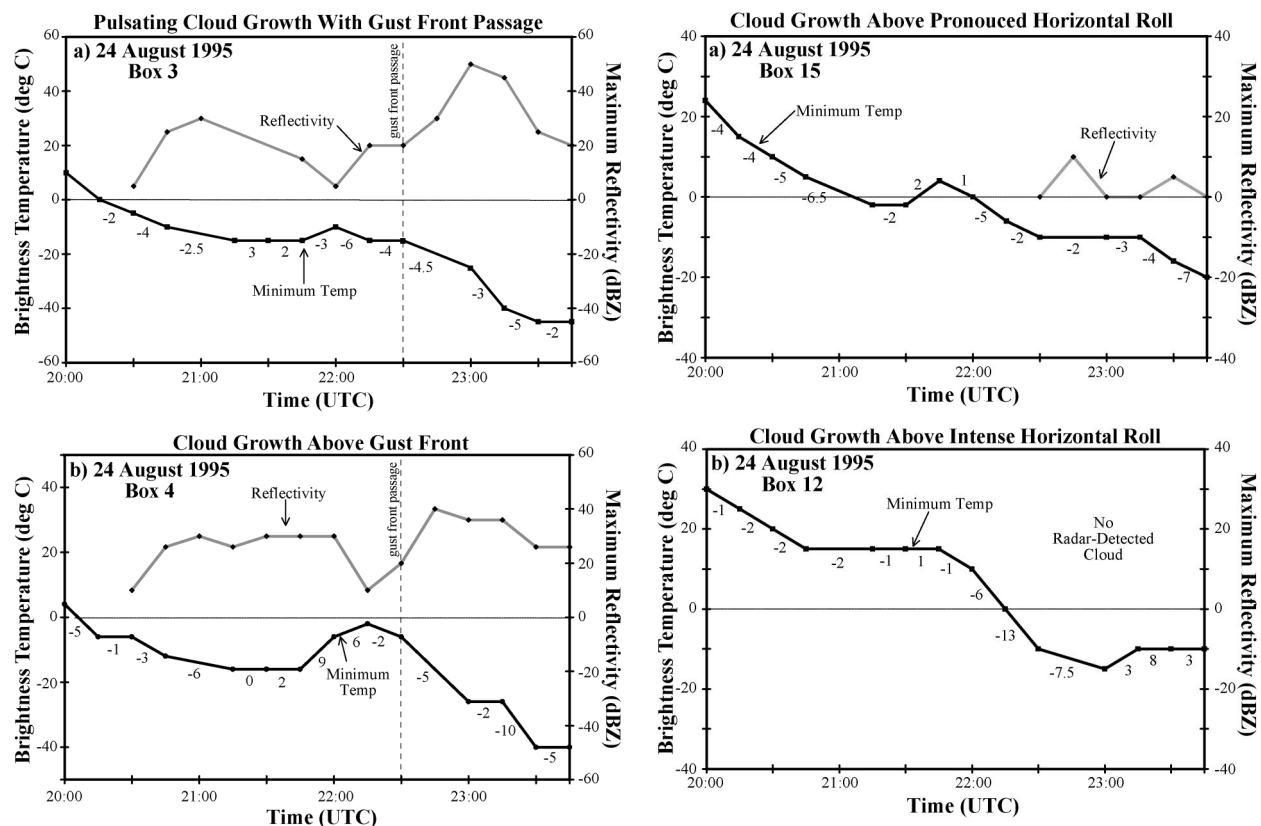


FIG. 8. Time series plots of IR brightness temperatures (black curve, °C) and maximum radar reflectivity (gray curve, dBZ) on 24 Aug for (a) pulsating cloud growth with gust front passage in box 3 in Figs. 7a,b and (b) cloud growth above gust front passage in box 4 in Figs. 7a,b. The ROC values over 15-min intervals are listed below the temperature curves. Vertical dashed line indicates time of gust front passage.

residence time of clouds near the source of strongest vertical motions; and 6) possible microphysical effects. In Mueller et al. (2003) and Saxen et al. (1999), all of the above components in addition to satellite are factored into nowcasting initiation, growth, and decay of thunderstorms.

2) GROWTH ABOVE HORIZONTAL ROLLS

Several NE–SW-oriented horizontal rolls were detectable by radar during the afternoon of 24 August. At 2230 UTC, they are located in the center of the subsectioned domain in Fig. 7b. In the areas defined by boxes 11, 12, and 15 in Fig. 7, significantly more cloudiness is observed within boxes 11 and 15 compared with box 12 and compared with most of the boxes in Fig. 7a. Figure 7b shows that a pronounced horizontal roll runs through boxes 15 and 12, while box 11 contains a less pronounced horizontal roll within its domain; a roll that dissipates as the afternoon progresses. A forecaster, using the visible imagery alone, might be tempted to focus in on these areas of cloudiness as specific re-

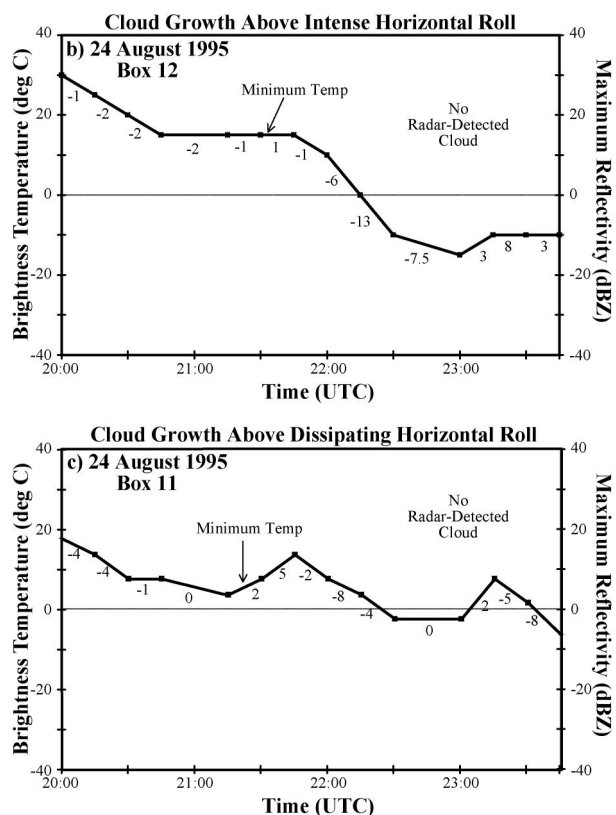


FIG. 9. Time series plots of IR temperatures (black curve) and maximum radar reflectivity (gray curve) on 24 Aug for (a) cloud growth above a horizontal roll within box 15 in Figs. 7a,b. (b) Cloud growth above a horizontal roll within box 12 in Figs. 7a,b. (c) Cloud growth above an adjacent, dissipating horizontal roll within box 11 of Figs. 7a,b. ROC values over 15-min intervals are listed below the temperature curves.

gions for nowcasting convective storm initiation. However, time series plots (Figs. 9a,c) show that the clouds percolated for quite awhile above the rolls: cooling, warming, then cooling, with no major cloud growth resulting as the cloud tops did not reach levels of significant subfreezing temperatures aloft. In Fig. 9b, a significant drop to subfreezing temperatures does occur at 2230 and 2300 UTC, but this trend does not continue

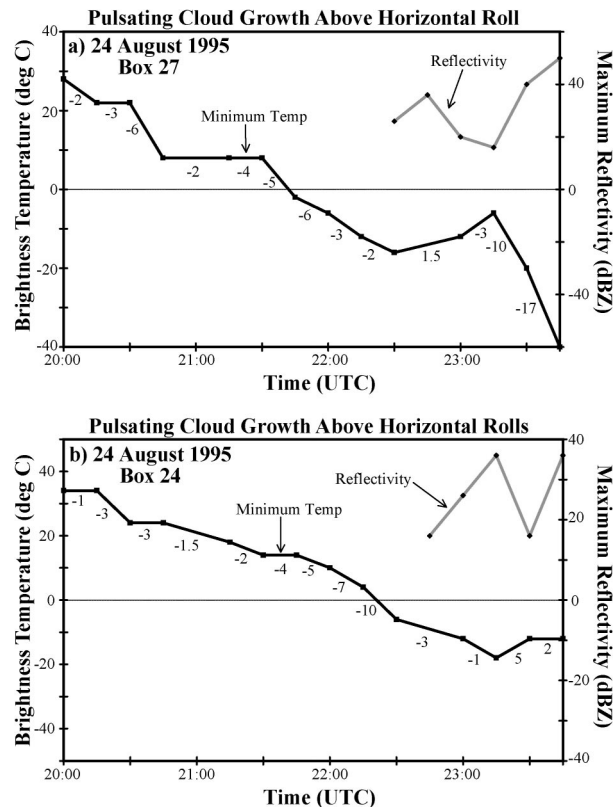


FIG. 10. Same as in Fig. 9 except for pulsating cloud growth above horizontal rolls within (a) box 27 and (b) box 24.

as cloud tops warm again to -10°C and no storms occurred. The lack of cloud growth within the cloudiest box, box 11, can be attributed in part to the dissipation with time of the source of vertical motion, the horizontal roll within its domain. The absence of precipitating storms within boxes 15 and 12 is likely a result of insufficient CBL moisture to sustain vigorous growth of clouds to produce storms; evidence for this can be seen in comparing these trends with those in Fig. 10.

On 24 August, surface mesonet stations available in northeastern Colorado showed that the air was more moist to the southeast of the radar and drier immediately to the northeast. These mesonet stations were spaced approximately 20–40 km apart; too coarse to provide detailed information on gradients of moisture convergence in the CBL but adequate for noting broad regions of moist and drier air. As a result of additional CBL moisture, the convection is more intense over the horizontal rolls within boxed regions 24 and 27 (Figs. 10a,b) as storms form following the drop to subzero cloud-top temperatures. It is important to note that the magnitude of the convergence (and inferred vertical motions), derived from the Tracking Radar Echoes by Correlation (TREC) cross-correlation tracker wind field, associated with these rolls was of equivalent intensity within both the northeastern and southeastern boxes.

Data from two additional cases, 21 and 24 July, are

discussed in this and the following subsection. Gridded domains were identified for each dataset and time series plots produced in the same manner as above.

On 21 July, a special sounding collected at 1700 UTC (Fig. 2c) contained only a modest amount of convective available potential energy (CAPE) compared to 23 and 24 August with a suggestion that convection might be capped by an elevated inversion near 400 mb. Available boundary layer moisture was less than that observed for the two August cases (see Fig. 2). The sounding represented a classic environment in Colorado for shallow, microburst-producing storms of moderate (40–45 dBZ) intensities (Wakimoto et al. 1994). The first available satellite image was at 1900 UTC (Fig. 7c) showing a mixture of cumulus and cumulus congestus clouds. The corresponding radar data at this time showed evidence that rolls were present but very weak (blue shades represent reflectivities from 3 to 10 dBZ) in the region defined by the overlaid grid (Fig. 7d) and less organized than observed in the cases already presented. At 2030 UTC, convection was already occurring with cumulus congestus clouds evident in the satellite visible imagery. What is informative about the set of time series data shown in Fig. 11 is how well the trends in the curves reflect conditions in the environment. The lack of strong, organized boundary layer convergence regions and little available CBL moisture coupled with the subsidence inversion aloft result in shallow, <25 dBZ convective storms whose cloud-top temperatures do not fall below -20°C until the end of the time period in Figs. 11a,b. In Fig. 11c, a steady and persistent drop in the trace of subfreezing temperatures is observed and moderate convective storm development occurs as temperatures drop to -40°C . The trend in Fig. 11c shows that potential for growth exists; it is not sufficient for a forecaster to rely on environmental conditions alone for storm nowcasting.

This case illustrates how ROC values shown in Figs. 11a–c can be used to discriminate between vigorous convection (large, negative rates) and suppressed convection (positive and very low negative values) once cloud tops have already reached subfreezing temperatures and the precipitation process has begun. The same result is seen in IR rate values in Fig. 12 from 24 July, a day with a strong capping inversion (Fig. 2d) at about 510 mb (-9°C) and another inversion at 460 mb (-15°C). Cloud tops are unable to cool much below -15°C and the rate of change in IR temperatures reflects this flat growth rate.

3) GROWTH AHEAD OF AND AT THE INTERSECTIONS OF ROLLS WITH GUSTS FRONTS

The most vigorous storm development by far was observed when gust fronts propagated into an area of horizontal rolls with the most intense convection occurring when the apex of the gust front was almost at right angles to the roll orientation. These findings are

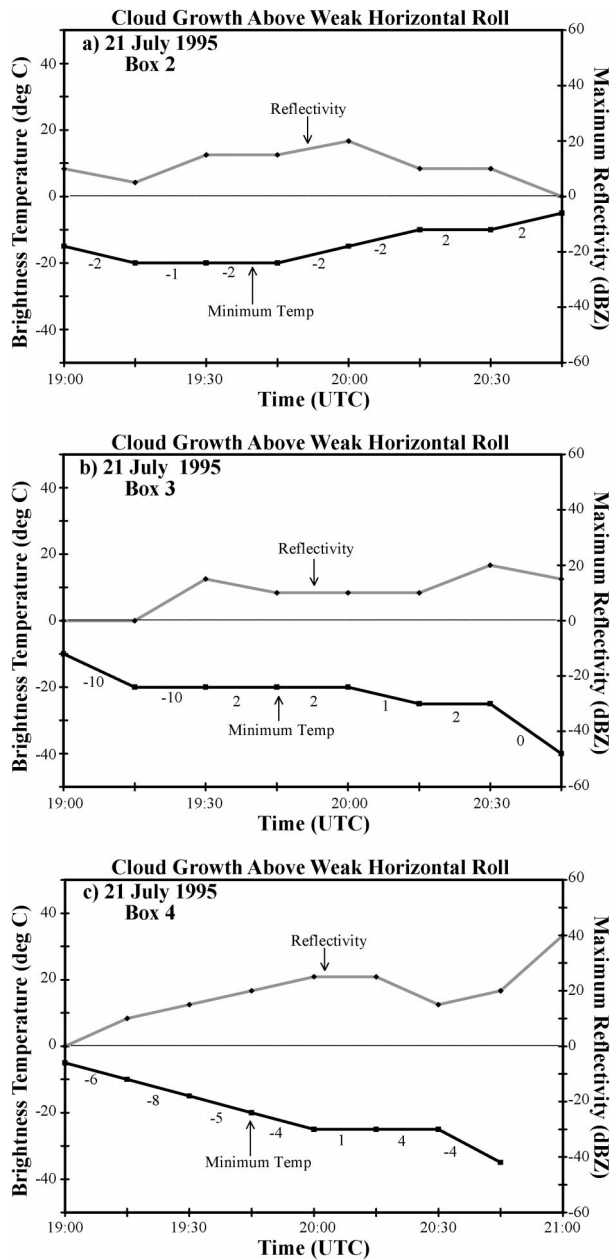


FIG. 11. Same as in Fig. 9 except for cloud growth above weak horizontal rolls on 21 Jul 1995 within (a) box 2 in Figs. 7c,d; (b) box 3 in Figs. 7c,d; and (c) box 4 in Figs. 7c,d.

consistent with the observations by Kessinger and Mueller (1991) of thunderstorm initiation in Florida. The temperature and reflectivity trends for 24 August (Fig. 13a) and 21 July (Fig. 13b) obtained from information in box 17 (see Figs. 7a,b) and box 1 (Figs. 7c,d), respectively, illustrate the drop to subfreezing temperatures 30–45 min before formation of first precipitation echoes, but with more intense ROC and larger reflectivity values than observed with the gust-front-only cases in Fig. 8. In Fig. 8, the additional vertical lift provided

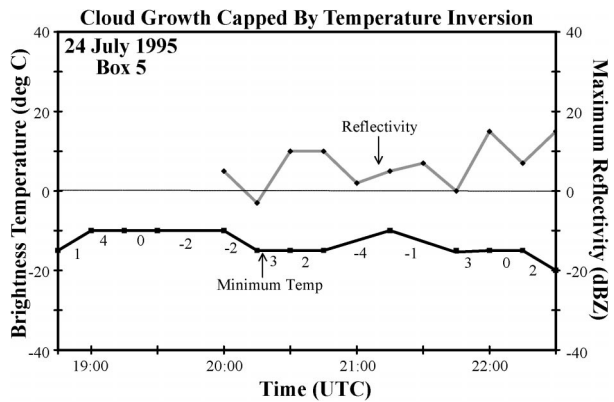


FIG. 12. Time series plots of IR temperature (black curve) and maximum radar reflectivity (gray curve) for cloud growth capped by temperature inversions. ROC values for 15-min intervals are listed below the temperature curve.

by the gust front is manifested in increased radar reflectivities, but the surge is not long lived (the maximum reflectivities decrease again with time) and lower ROC values reflect the lack of sustained growth. Comparison

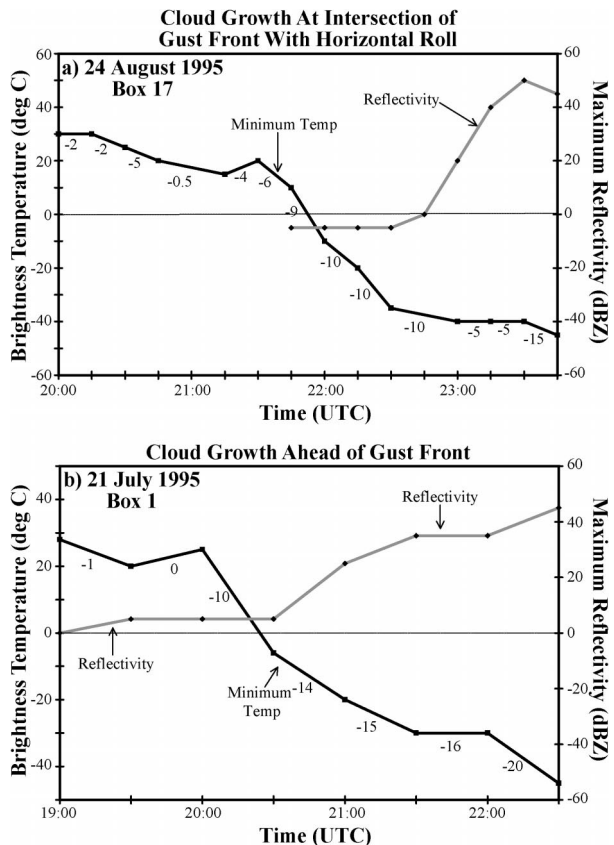


FIG. 13. Time series plots of IR temperature (black curve) and maximum radar reflectivity (gray curve) for (a) cloud growth above gust front interactions with horizontal rolls on 24 Aug within box 17 in Figs. 7a,b and (b) cloud growth ahead of an approaching gust front on 21 Jul within box 1 in Figs. 7c,d.

TABLE 1. List of satellite algorithms running in the ANC system.

Satellite algorithms	Function	Objective
SatParallax	Correct for parallax error	Alignment of convective clouds with radar signatures
Satellite filtering	Masks out undesired information	To remove nonconvective cloud and very cold anvil regions from data prior to computing IR rate field
CloudClass	Classify types of clouds	To detect regions of cumulus clouds
RateOfChange (ROC)	Advects satellite data and computes change in IR temperature with time	To detect and monitor early growth of clouds

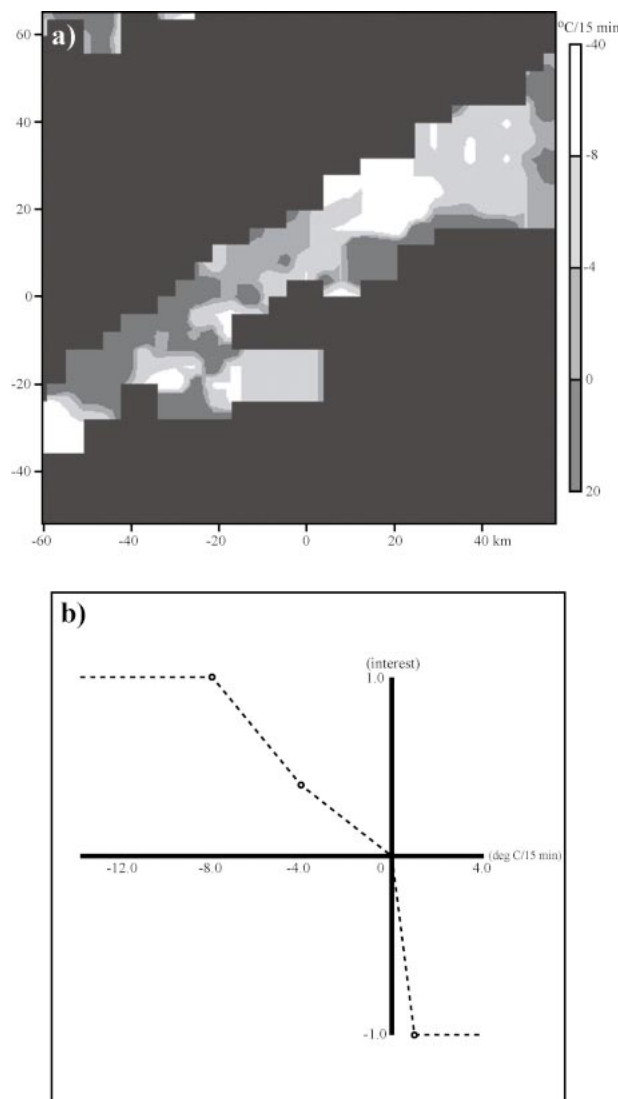


FIG. 14. Example of how a membership function derived from observations and forecaster experience is applied to a satellite data field for transformation into a likelihood field. (a) The temperature rate of change field (gray shades, $^{\circ}\text{C}$) computed over approximately 15-min intervals from 2 Jun 2000; (b) membership function (dashed curve) derived from results in section 3. Temperatures $< -8^{\circ}\text{C}$ in (a) would be assigned a high interest value of 1 in the resulting, gridded likelihood field.

of the trends in Fig. 13 with those for growth above gust fronts (Fig. 8) and above horizontal rolls (Figs. 9, 10, and 11) suggests that one can categorize the type of cloud growth based on both subzero cloud-top temperature and ROC values. ROC values within -8° to -4°C represent weak, limited growth and values $< -8^{\circ}\text{C}$ are associated with growth that will lead to more intense storms. These numbers have been used in the ANC system (Mueller et al. 2003) to define the membership functions for storm initiation as described in the following section.

4. Operational applications and considerations

The suite of operational datasets available to NWS forecasters in weather forecast offices are the same datasets used by the ANC nowcasting system described by Mueller et al. (2003). This system applies several algorithms (synchronized in real time) to these data to identify boundary layer, cloud, storm, and environmental features related to thunderstorms. Through the use of membership functions (McNeill and Freiberger 1993) features and precursor signatures important to thunderstorm initiation, growth, and decay are assigned interest or likelihood values ranging from -1 (low likelihood) to 1 (high likelihood). Weighted likelihood fields are then combined to produce the final thunderstorm nowcast field. Algorithms that process satellite data in the ANC system are listed in Table 1. Although the satellite-based likelihood fields from these algorithms are available for display, forecasters generally preferred to view only the final nowcast fields.

Figure 14 illustrates how a cloud growth likelihood field is obtained for use in the ANC system. ROC thresholds from section 3b(3) and corresponding interest values define a membership function, shown in Fig. 14b, that can be applied to a gridded ROC field (Fig. 14a). The resulting likelihood field has a similar look to Fig. 14a, except that the gridded values are now interest values rather than rate values. Highest likelihoods are in regions of greatest cooling (values $< -8^{\circ}\text{C}$; lighter gray and white shades) calculated over approximately 15-min intervals. Regions of temperature warming (values > 0) are assigned negative values and the likelihood for new storm initiation is suppressed in those gridded areas. This same methodology is used to convert gridded cloud classification (Bankert 1994; Roberts et al. 1999;

Tag et al. 2000) and cloud temperature fields to likelihood images, using appropriate threshold limits for the abscissa in the membership functions.

To illustrate the relative value of including satellite likelihood fields in the ANC system, two cases are presented from two very diverse geographical regions of the United States. The first case is taken from the ANC system that was used at the Washington, D.C.–Baltimore, Maryland, Weather Forecast Office (WFO) in Sterling, Virginia, for four summers from 1997 to 2000, in conjunction with the National Weather Service's System for Convection Analysis and Nowcasting (SCAN; Smith et al. 1998; Roberts et al. 1999) project. The second case is from a permanent ANC system in use at the Weather Forecast Office at the White Sands Missile Range (WSMR) in New Mexico since 1997 (Saxen et al. 1999). An overview on the use of the ANC system by forecasters at both Sterling and White Sands is documented in Roberts et al. (1999).

a. Satellite sensitivity studies on nowcasts produced at an NWS Forecast Office

In this section we show a case from the ANC system that ran at the Washington, D.C., WFO to demonstrate the contributions of specific satellite likelihood fields toward the accuracy of the convective storm nowcasts. These likelihood fields include the cloud-classification and ROC fields. The accuracy of the nowcasts when all likelihood fields are included in ANC is also presented.

On 2 June 2000, a cold front located in Pennsylvania was approaching Virginia and was expected to arrive in the Washington, D.C., area at about 2100 UTC. Forecasters (S. Zubrick and J. Margraf 2000, personal communication) were anticipating convection associated with the arrival of the cold front and their focus was not on a quasi-stationary, mesoscale convergence boundary located 40 km immediately NW of the WFO evident in radar and satellite imagery. A strengthening of the surface convergence along this boundary, as inferred from the intensification of the radar thin line and velocity fields, occurred as it slowly moved southeastward toward the WFO. The growth of cumulus clouds above the boundary was evident in the visible imagery at 2215 UTC in Fig. 15 (Fig. 18 shows a sequence of visible imagery from 2130 to 2200 UTC). Prior to 2215 UTC, no precipitation echoes were present aloft. The 30-min nowcasts for >35 dBZ storms produced in real time at the WFO at four successive time periods starting at 2155 UTC are shown in Figs. 16e–h. These nowcasts, which included information from satellite cloud-classification predictor fields, are overlaid onto the radar reflectivity image at nowcast time and overlaid onto the reflectivity images at nowcast validation time in Figs. 16i–l. The primary likelihood fields contributing to these nowcasts included favorable boundary layer features surrounding the mesoscale boundary and detection of favorable cloud-top temperatures and cumulus clouds

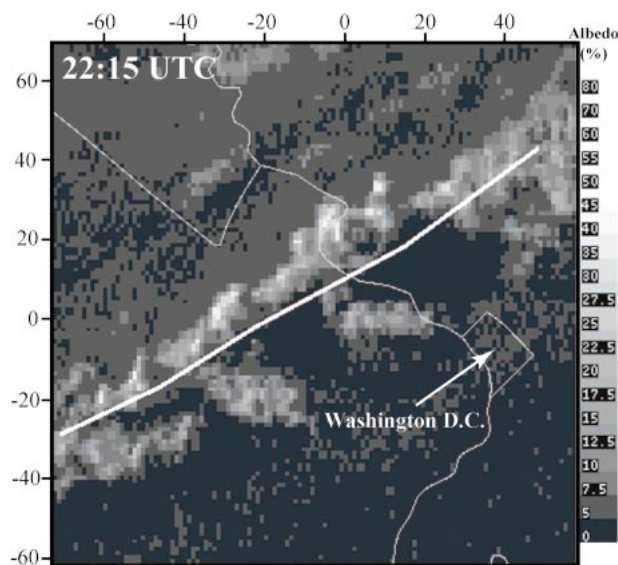


FIG. 15. GOES-8 visible image of the growing cloud line approaching Washington, DC, at 2215 UTC 2 Jun 2000. The solid white line is the location of the mesoscale convergence boundary as seen on radar.

from the satellite data. For comparison purposes, the 30-min nowcasts produced without satellite information are shown in Figs. 16a–d for the same time sequence. It can be seen in the second column of images in Fig. 16 that a NE–SW line of storms are nowcast to occur over the D.C. area in the next 30 min. Indeed, as the validation panels show, a continuous line of intense storms initiated in this area well ahead of the expected cold front, which had stalled in Pennsylvania. Without the contribution of the satellite information, the ANC system would have underforecast the total extent of the developing line as illustrated by the very few polygons in Figs. 16c,d and missed the extra 30-min lead time for forecasting the initiation of the squall line, Figs. 16a,b.

A statistical comparison of the nowcasts with the observed fields at every grid point is shown in Fig. 17. The observed (verification) field at nowcast validation time is the radar reflectivity field at a constant altitude level of 1.5 km AGL. Reflectivities greater than 35 dBZ are delineated as regions of storms. Using the contingency table approach discussed by Doswell et al. (1990) the probability of detection (POD), false alarm ratio (FAR), and critical success index (CSI) have been computed and are plotted in Fig. 17. The magnitudes of the statistics are quite dependent upon how the statistics are computed. In this case a 1-km grid-to-grid comparison is very stringent and individual magnitudes are not particularly meaningful by themselves. It is more informative to compare these statistical results against other baseline measures of performance. In Fig. 17, storm extrapolation statistics, obtained by evaluating the performance of storm location forecasts from the TITAN

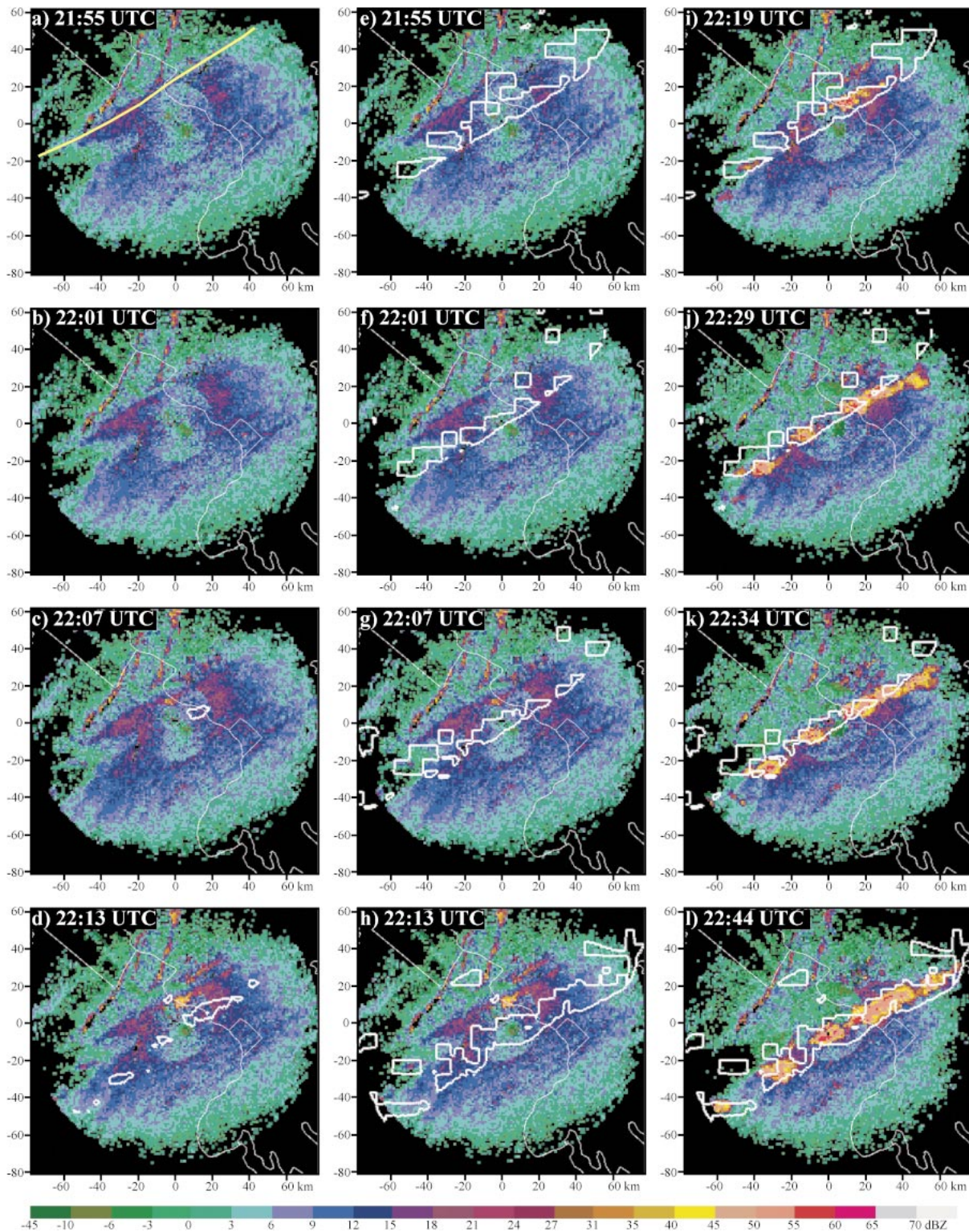


FIG. 16. Time series comparison of (a)–(d) 30-min nowcasts of reflectivities >35 dBZ (white polygons) based on radar only parameters and (e)–(h) those that included satellite cloud-classification predictor fields. (i)–(l) Verification reflectivity field with overlying satellite-based nowcast polygons from (e)–(h). Underlying field is radar reflectivity for 2 Jun 2000 from the Sterling, VA, WSR-88D. The solid yellow line in (a) is the location of the mesoscale convergence boundary at 2155 UTC.

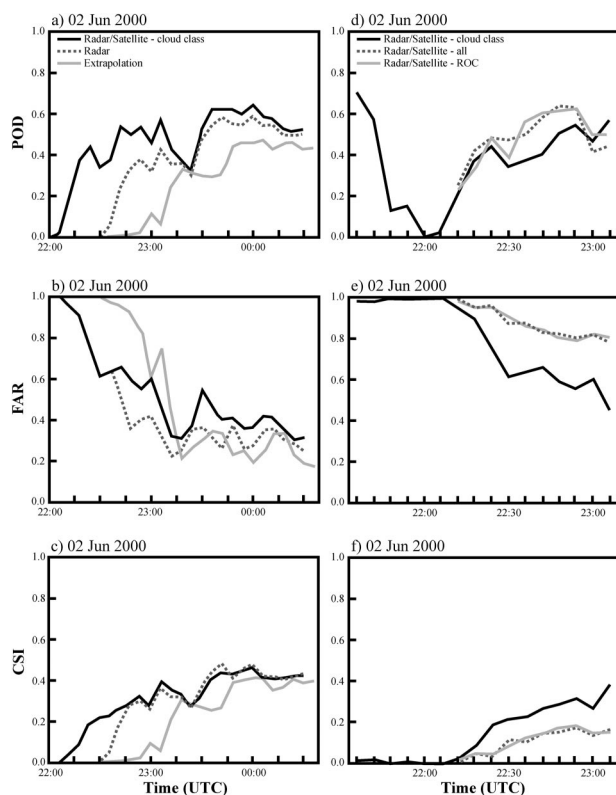


FIG. 17. Verification statistics for 30-min nowcasts produced when different satellite likelihood fields are included in the ANC system for 2 Jun 2000 at Sterling, VA. Time listed along abscissa is validation time. The black curve is performance of nowcasts run in real time using both radar and the satellite cloud-classification likelihood fields (a)–(c) during the evolution of the storms from 2200 to 0045 UTC, and (d)–(f) during the period of initiation and growth of the storms from 2130 to 2300 UTC.

storm track algorithm (Dixon and Wiener 1993), are provided as a benchmark for comparison with the ANC runs. The radar–satellite statistics are for nowcast runs using radar-based and the satellite cloud-classification likelihood fields. The same radar-based information is used for radar-only nowcasts. The 30-min lead time that the satellite information provides in predicting storm initiation can be seen by comparing the ANC radar–satellite curves in Figs. 17a,c against the radar-only and storm extrapolation curves.

To address the sensitivity of the 30-min nowcasts to different satellite interest features, the nowcasts discussed above using the cloud-classification likelihood field and nowcasts produced using the ROC likelihood field are both plotted in Fig. 18, overlaid on the radar data at the nowcast verification time. The radar-based information used in both nowcasts are identical, so the differences observed between the nowcasts are due only to the satellite likelihood field used. The time sequence shown, 2130–2200 UTC, spans the period of rapid growth of the cloud line, as is reflected in the visible imagery and 30-min advected ROC fields in Fig. 18.

Clearly evident is that the cloud-classification-based nowcasts do a good job at predicting the development of a line of storms but result in false alarms along the NE and SW portions of the line (Fig. 18k) where the growth rate is minimal. In contrast, the ROC-based nowcasts are located only in those areas where the temperature change is large (Figs. 18h,i) and thus the overwarning is reduced. The ROC-based nowcasts also do well at nowcasting the initiation of the line (remember from Fig. 16 that no storms exist on radar at these nowcast times) but tend to overwarn in areas immediately perpendicular to the line (Fig. 18i). Most of this overwarning is a direct result of the accuracy in advection of cloud features prior to computation of the ROC field. Not only must the most representative motion vector or cross-correlation vectors be applied to the satellite imagery for calculation of an accurate rate field, but this field must then be advected 30 min into the future to line up with other fields used in a 30-min storm nowcast.

There is concern that inclusion of satellite information could cause extensive overwarning or false alarm nowcasts particularly during the nascent stage of cloud growth between 2130 and 2300 UTC. However, it is clear in the first time period shown in Fig. 18g that the ROC field substantially reduces the number of false alarms. In fact, there is no nowcast issued at all. At 2130 UTC (Fig. 18d), the ROC values are primarily in the range of -2° to $-8^{\circ}\text{C}/15\text{ min}$. In the ANC system, values of ROC must exceed $-8^{\circ}\text{C}/15\text{ min}$ in order to have high likelihood values that contribute significantly to the thunderstorm initiation nowcast (see Fig. 14b). Based on examination of numerous cases from the Washington, D.C., area, this ROC value has proved to be a reliable threshold for convection initiation nowcasts. Thus no nowcast areas are generated at 2130 UTC validating at 2200 UTC (Fig. 18g) using ROC information compared to the large false alarm regions produced using the cloud-classification data (Fig. 18j). This is also apparent in the verification statistics shown in Figs. 17d–f comparing performance of the nowcasts that used the ROC field with the nowcasts that used the cloud-classification field. The use of ROC in the nowcast eliminates all the early overwarning and false alarms in the verification period between 2130 and 2206 UTC (Fig. 17e).

Additional incremental performance is obtained in predicting convection initiation when all the satellite likelihood fields are included in the ANC nowcasts (radar/satellite-all curve in Fig. 17d). The CSI skill decreases some during this same period of storm initiation and growth due to slightly higher FAR numbers and the very strict, grid-to-grid validation methodology employed. But from a qualitative sense as can be seen in Fig. 18, the satellite information provides significant cant added value in being able to nowcast those first intensifying storms.

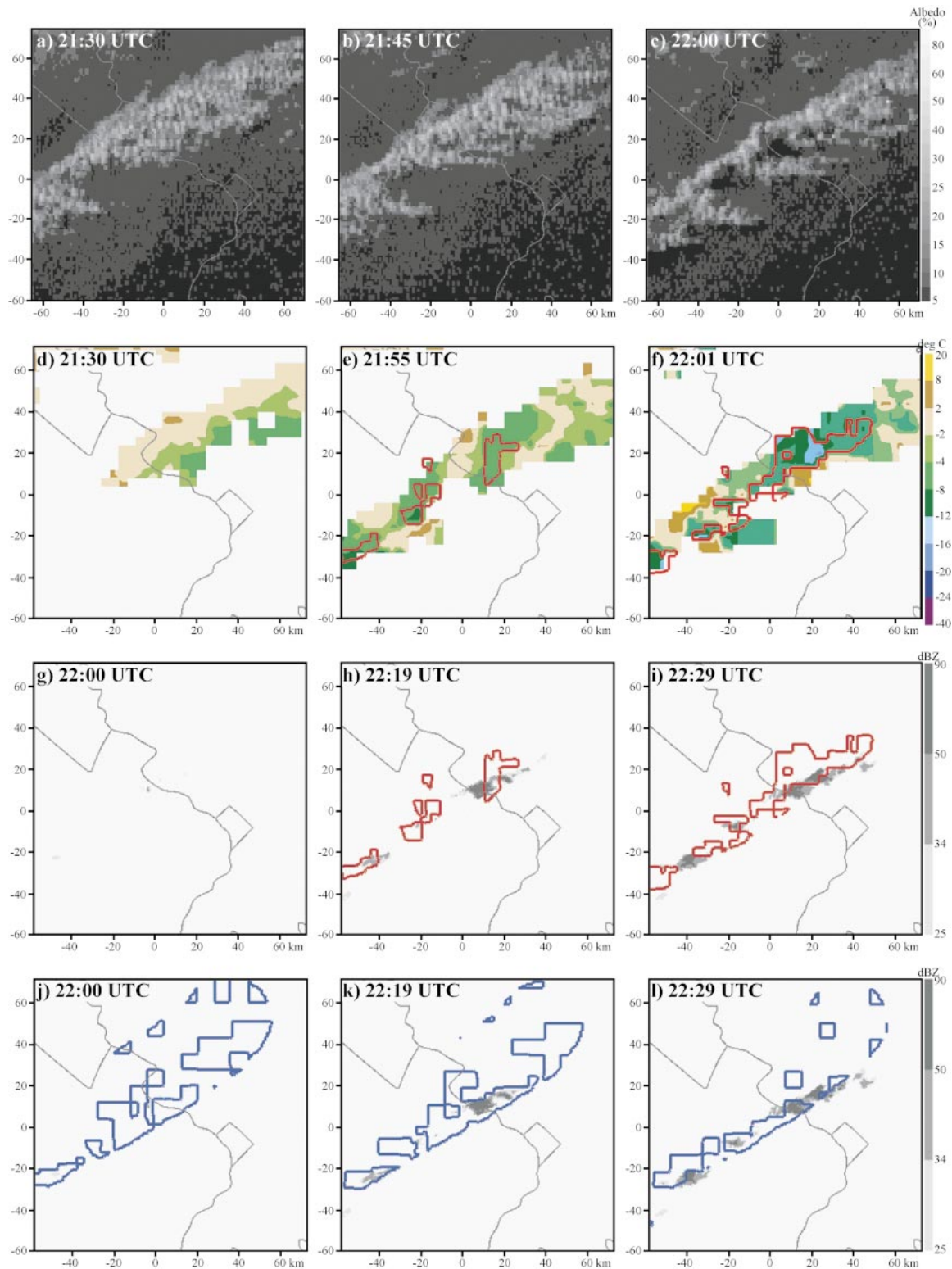


FIG. 18. Performance of two different satellite-based, 30-min nowcasts (red vs blue polygons) at three forecast times on 2 Jun 2000. (a)–(c) Visible *GOES-8* at nowcast times; (d)–(f) advected ROC field (colored field) with overlaid 30-min nowcasts (red polygons) that included the ROC predictor field; (g)–(i) reflectivity plots at verification time (gray shades) with the 30-min nowcasts from (d)–(f) overlaid (red polygons); and (j)–(l) same as (g)–(i) except overlaid nowcasts (blue polygons) based on cloud-classification predictors. See text for explanation.

b. Nowcasts produced at WSMR Weather Forecast Office using combined satellite and radar interest fields

In this section, real-time nowcasts produced using the full suite of satellite and radar likelihood fields are presented for a case from White Sands, New Mexico. This case also illustrates the benefit satellite information provides in nowcasting convection initiation over complex terrain.

In the area surrounding White Sands, storms tend to form above two semiparallel N–S-oriented mountain ranges separated by a valley (see Fig. 19) where WSMR is located. On 27 July 2001, a gust front produced by storms over the eastern range traversed the valley, converging onto the slopes of the western range resulting in upslope flow and the formation of thunderstorms along the western range. The primary features contributing to the storm nowcasts include characteristics of the CBL environment surrounding the gust front, terrain effects, detection of cumulus clouds and clear sky, cloud-top temperatures, and cloud-top cooling rates. Convection frequently initiates over the mountains; thus, a terrain interest field is included in the ANC system (see Saxen et al. 1999 for details). Two sets of 30-min nowcasts are discussed here. 1) The nowcasts produced using both satellite and radar information (red polygons in Fig. 19) in real time. Radar information plus a favorable combination of cloud-top temperatures between 0° and –20°C, “CloudClass” (see Table 1), and ROC features must be met for a 30-min nowcast to be generated. 2) The nowcasts produced in postanalysis with satellite information excluded from the ANC system (black polygons in Fig. 19).

Issues arise when using satellite information in a real-time operational nowcast product on how best to combine 15-min satellite updates with 6-min radar update frequencies. Figure 19 highlights how this is handled in the ANC system. At the 1836 UTC nowcast time the 1815 UTC satellite information is used. For the 1845 and 1851 UTC nowcast times, the 1845 UTC imagery and corresponding ROC information are used in both nowcasts. Subtle differences are observed in the red polygons between the two time periods due to updates in the radar information and how these weighted fields combine with the same satellite information. Upstream processing of satellite data (e.g., parallax correction, filtering, and cloud advection schemes) is also necessary and has a direct impact on the accuracy of the nowcasts. The ROC field in Fig. 19 illustrates the benefits of this processing where temperature rates exist only in regions of cumulus and cumulus congestus clouds and not in regions of anvil, mixed cloud types, and clear sky.

At the start of this event at 1836 UTC, only one storm echo is present in the valley between the mountain ranges and both methods produce identical nowcasts for this storm to persist indicating this is primarily a radar-based nowcast. The GOES visible image at 1815 UTC shows

cumulus clouds were present in the vicinity of the outflow boundary and above the higher terrain; the CloudClass field (not shown) accurately classifies this region with cumulus clouds and clear sky. However, the ROC field shows no marked cooling of clouds except over the Sacramento Mountains where mature storms exist and the cloud tops in the valley region have not reached subfreezing temperatures. By 1845 UTC, a marked change has occurred in the satellite imagery; the line of cumulus clouds in the valley has undergone significant development. All along this line, temperature changes exceed $-8^{\circ}\text{C}/15\text{ min}$, the minimum threshold used for vigorous storm development. As a result of the ROC information, the 30-min nowcast (red) polygons at 1845 and 1851 UTC extend well to the north and to the south of the radar-based nowcast into areas of no radar echo aloft. These storm initiation nowcasts are impressive for how well they verify 30 min later (see Figs. 19e,f). The POD statistics during this 15-min period, Fig. 20a, show a significant improvement in accuracy from 0.25 for the radar-based nowcast to 0.85 when satellite information is included, with very little impact overall on the FAR scores (Fig. 20b). The CSI scores (Fig. 20c) also reflect the improvement in skill during this period. A comprehensive set of statistics for the ANC systems running at the Washington, D.C., WFO and WSMR forecast offices is given in Mueller et al. (2003).

In complex terrain, the radar beam is blocked at low altitudes making it difficult to detect convergence boundaries and harder for the ANC system to predict convection initiation. Thus, detection of cloud growth on satellite becomes more important over complex terrain. In Fig. 21, new storms develop over the mountains at 1928 UTC. ANC does quite well in nowcasting the new initiation over the mountains, starting at 1910 UTC with discrete cellular nowcasts and evolving into nowcasts at 1928 UTC for a line of storms that indeed did develop by 1958 UTC. Clearly the inclusion of satellite information has provided added value and accuracy to the convection initiation nowcasts. This was true also for nowcasts produced by the system over the complex terrain located west of the Washington, D.C., WFO, even though the nowcast domain included only a very small portion of the foothills of the Appalachian Mountains.

5. Conclusions

This study has examined cloud growth that occurred on four different days in Colorado and on two selected days in the vicinity of Washington, D.C., and White Sands, New Mexico, as part of a real-time system that produces nowcasts of convective storms. A wealth of data was collected and analyzed in these areas during the warm season. They showed similar growth tendencies as in the cases presented here. Only a small subset of data was presented here to demonstrate the concept of using combined satellite and radar data for monitor-

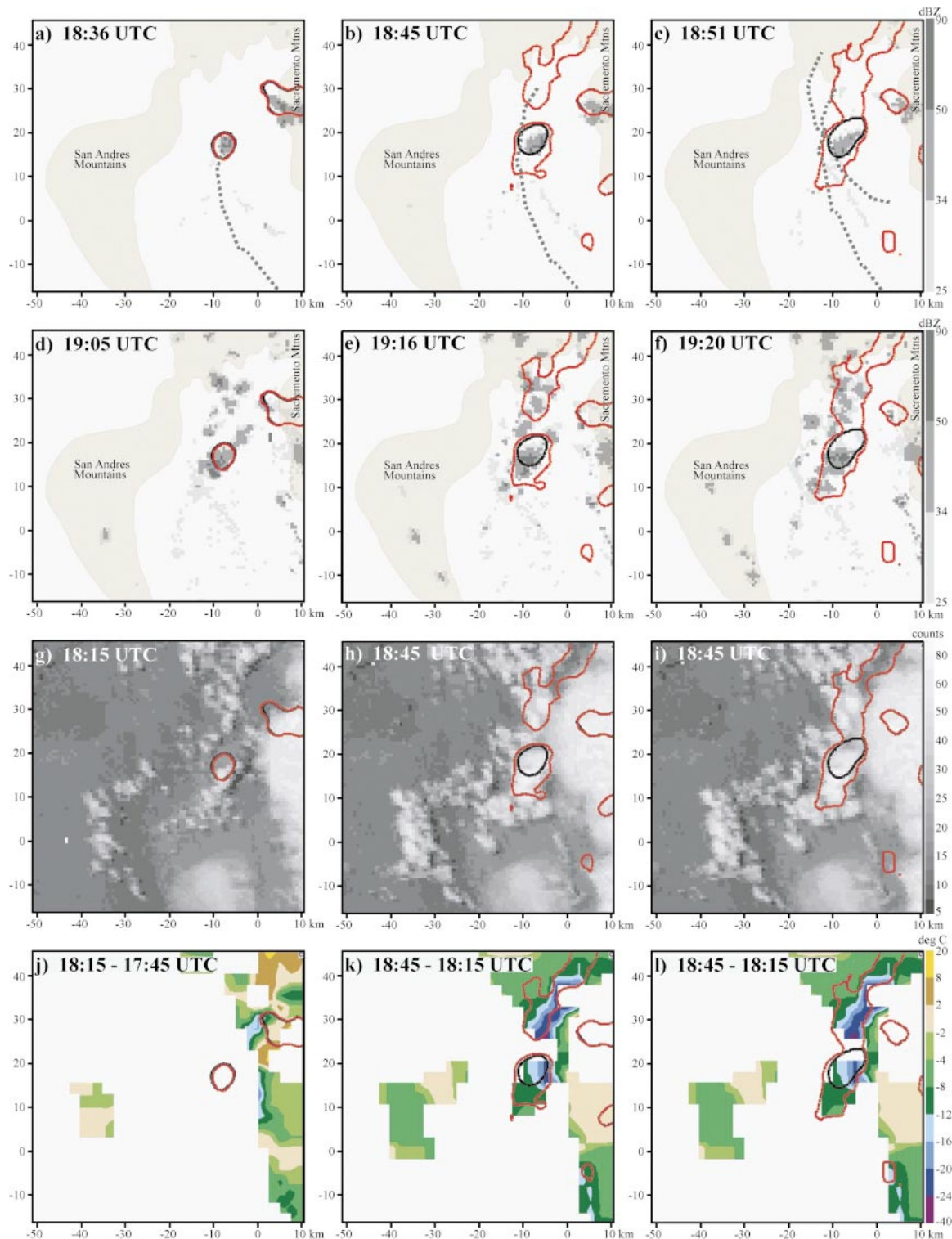


FIG. 19. Comparison of 30-min nowcasts at three different time periods with (red polygons) and without (black polygons) satellite data for 27 Jul 2001 from White Sands, NM. (a)–(c) Radar reflectivity at nowcast times 1836, 1845, and 1851 UTC; (d)–(f) radar reflectivity at nowcast verification times 1905, 1916, and 1920 UTC; (g)–(i) satellite visible imagery at nowcast time; and (j)–(l) ROC fields at nowcast time. The dashed lines are the 30-min extrapolated, surface convergence boundary locations.

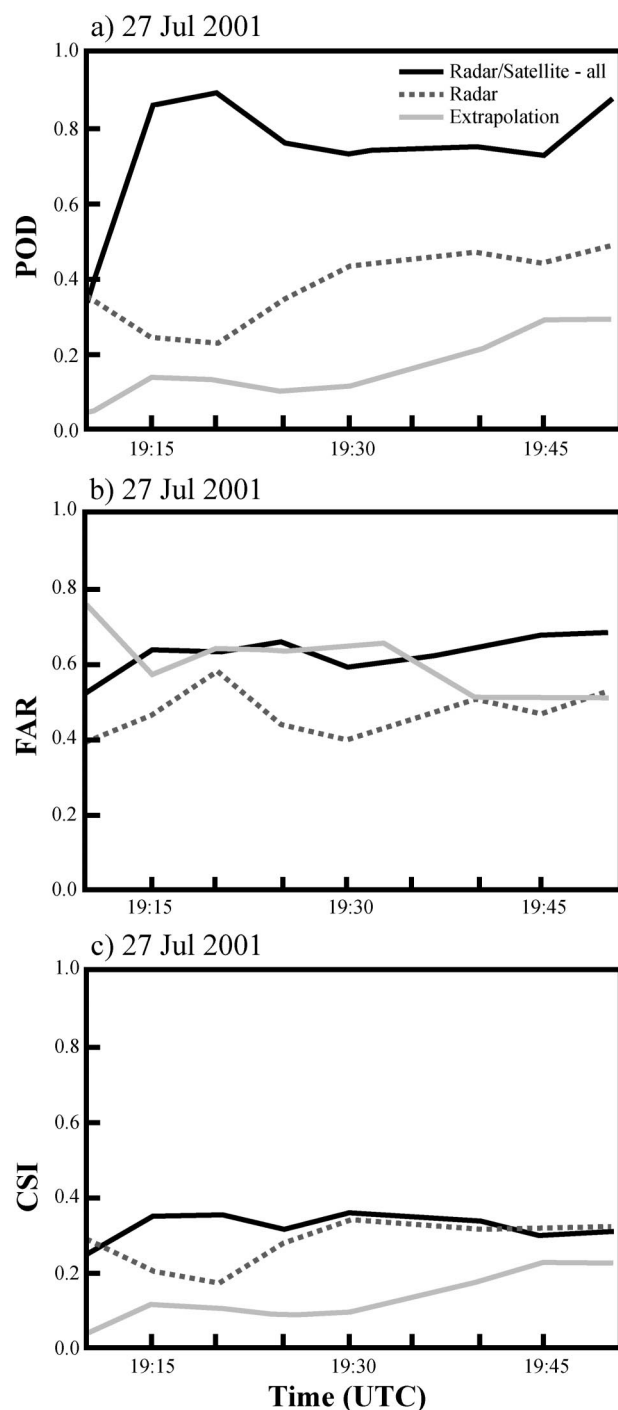


FIG. 20. Comparison of verification statistics for two sets of ANC nowcasts run for WSMR on 27 Jul 2001 against nowcasts based on storm echo extrapolation (gray solid curve). Time listed along abscissa is validation time.

ing cloud growth and to illustrate how this approach has been employed in a real-time system for nowcasting convective storms. Nocturnal convection was not considered in this study due to the difficulty in distinguish-

ing cumulus clouds from surface radiation in the IR imagery.

This study has demonstrated that satellite imagery data can quantify cloud growth in the vicinity of boundary layer convergence features and above complex terrain. The more intense convection and storm development observed on satellite was directly tied to regions of enhanced convergence in the boundary layer detected by radar, that is, gust front passage, gust front intersections with horizontal rolls, and terrain-induced convergence. *By examining the satellite-based, cloud growth rates (i.e., temporal change of cloud-top temperatures) associated with a variety of surface convergence features, we have been able to define threshold values in these cases that demarcate transitions between suppressed, active, and vigorous convection.* These threshold values define the initial points of a membership function used to produce temperature rate of change likelihood fields in the NCAR convective storm nowcasting system (ANC; Mueller et al. 2003).

Tracking cloud growth rates and monitoring the drop in satellite cloud-top temperatures from 0° to -20°C proved to be important precursor information to storm initiation in the cases presented. It is assumed that once clouds grow to a height where the cloud tops radiate at subfreezing temperatures, the ice nucleation process and the development of precipitation are likely initiated in these cold-type continental clouds. A relationship was observed between satellite and radar data during this critical period. Following the drop to 0°C on satellite, approximately 15 min was observed to elapse before a precipitation echo (>5 dBZ) was detected on radar. As the clouds continued to cool an additional 15 min elapsed before echoes >30 dBZ were observed, 30 or 35 dBZ being the typical reflectivity thresholds used to track the movement of thunderstorms. *Thus, by monitoring via satellite both the cloud growth rate and the occurrence of subfreezing cloud-top temperatures, the potential for up to 30 min of advance notice of convective storm initiation over the use of radar alone is possible.*

In addition to a satellite-based cloud classification algorithm, algorithms utilizing the above results have been implemented as part of the ANC guidance system at two operational forecast offices. It has been shown here for the Washington, D.C., and White Sands cases that *inclusion of satellite information increased the lead time and accuracy of the automated convective storm initiation and growth nowcasts compared to nowcasts based on radar information alone.*

Acknowledgments. The authors would like to thank James Wilson, Cindy Mueller, and Roy Rasmussen for their comments on an earlier version of this paper. We are grateful to Dan Megenhardt for his assistance with the figures; to Matt Meister and Tom Saxen for their assistance with the 2 June and 27 July datasets, respectively; and to Laurie Carson and Niles Oien for

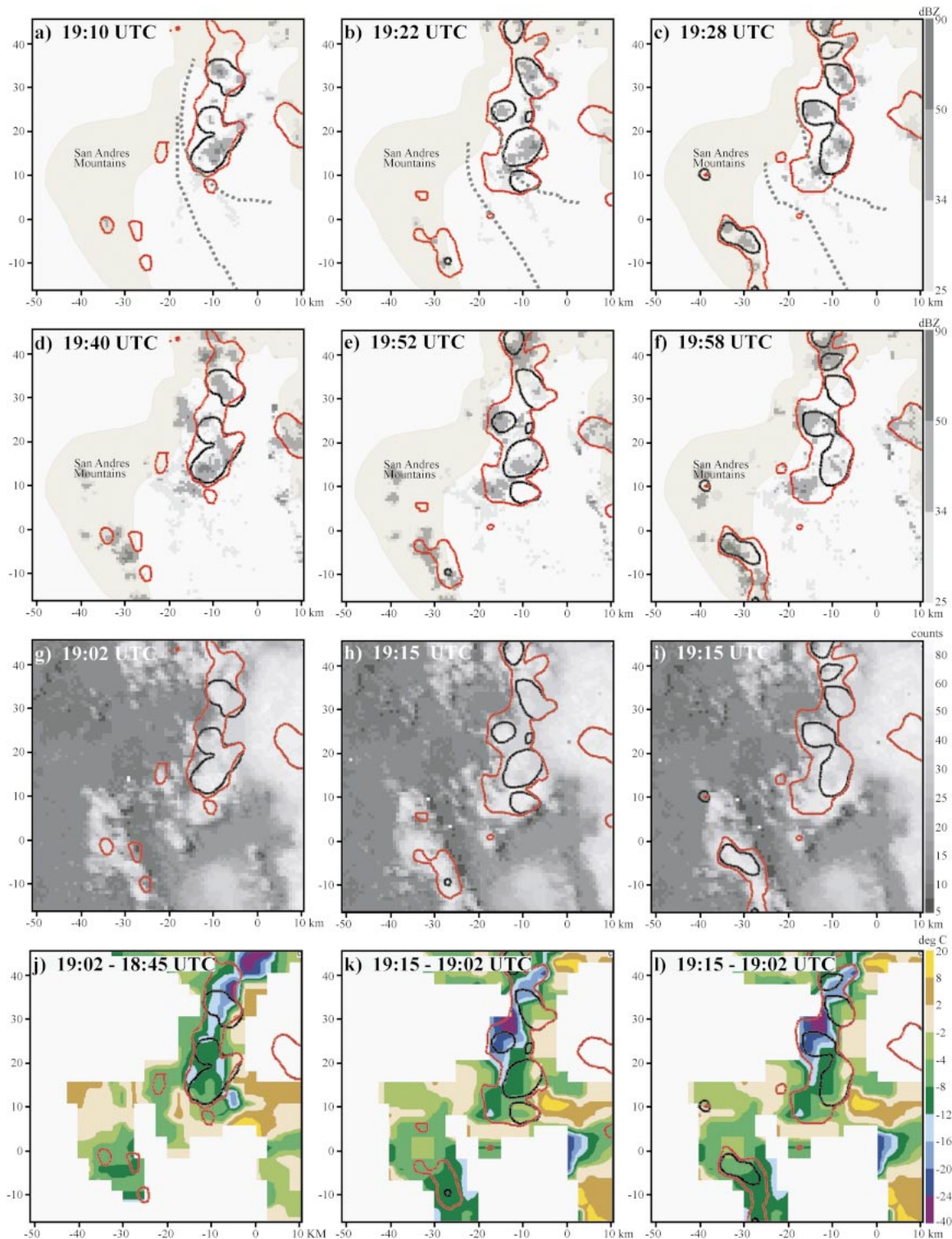


FIG. 21. Same as in Fig. 19 except at three later nowcast times of 1910, 1922, and 1928 UTC.

software development. The FAA Aviation Weather Research Program, particularly Dave Pace, has provided continued support of the development of the ANC system through Interagency Agreement 98C00031. The Army Test and Evaluation Command has supported the installation and operation of the ANC at White Sands Missile Range. The U.S. Weather Research Program and the Nexrad Operational Support Facility, particularly James Belville and Donald Burgess, supported the running of the ANC system at the Washington WFO during SCAN. This work was also supported by a grant from the National Science Foundation to Colorado State University, ATM-9726464. Steven Zubrick, the NWS SOO at the Sterling WFO and forecaster John Margraf are thanked for their analysis and reconstruction of the 2 June synoptic and mesoscale events; Eric Hatfield is acknowledged for providing valuable forecaster input on the ANC system running at White Sands.

REFERENCES

- Atkins, N. T., R. M. Wakimoto, and T. M. Weckwerth, 1995: Observations of the sea-breeze front during CaPE. Part II: Dual-Doppler and aircraft analysis. *Mon. Wea. Rev.*, **123**, 944–969.
- , —, and C. L. Ziegler, 1998: Observations of the finescale structure a dryline during VORTEX 95. *Mon. Wea. Rev.*, **126**, 525–550.
- Bankert, R. L., 1994: Cloud classification of AVHRR imagery in maritime regions using a probabilistic neural network. *J. Appl. Meteor.*, **33**, 909–918.
- Boyd, J. G., 1965: Observation of two intersecting radar fine lines. *Mon. Wea. Rev.*, **93**, 188.
- Browning, K. A., and C. G. Collier, 1982: An integrated radar-satellite nowcasting system in the UK. *Nowcasting*, K. A. Browning, Ed., Academic Press, 47–61.
- Byers, H. R., and R. R. Braham Jr., 1949: *The Thunderstorm*. U.S. Govt. Printing Office, 287 pp.
- Christian, T. W., and R. M. Wakimoto, 1989: The relationship between radar reflectivities and clouds associated with horizontal roll convection on 8 August 1982. *Mon. Wea. Rev.*, **117**, 1530–1544.
- Collier, C. G., and R. B. E. Lilley, 1994: Forecasting thunderstorm initiation in north-west Europe using thermodynamic indices, satellite and radar data. *Meteor. Appl.*, **1**, 75–84.
- Crook, N. A., T. L. Clark, and M. W. Moncrieff, 1990: The Denver cyclone. Part I. Generation in low Froude number flow. *J. Atmos. Sci.*, **47**, 2725–2742.
- Dixon, M., and G. Wiener, 1993: TITAN: Thunderstorm Identification, Tracking, Analysis and Nowcasting—A radar-based methodology. *J. Atmos. Oceanic Technol.*, **10**, 785–797.
- Doswell, C. A., III, 1980: Synoptic-scale environments associated with high plains severe thunderstorms. *Bull. Amer. Meteor. Soc.*, **61**, 1388–1400.
- , R. Davies-Jones, and D. L. Keller, 1990: On summary measures of skill in rare event forecasting based on contingency tables. *Wea. Forecasting*, **5**, 576–585.
- Dye, J. E., and B. E. Martner, 1982: The 26 July 1976 case study: Microphysical observations. *Hailstorms of the Central High Plains*, C. A. Knight and P. Squires, Eds., Vol. 2, Colorado Associated University Press, 211–228.
- , W. P. Winn, J. J. Jones, and D. W. Breed, 1989: The electrification of New Mexico thunderstorms. Part I. Relationships between precipitation development and the onset of electrification. *J. Geophys. Res.*, **94**, 8643–8656.
- Fankhauser, J. C., N. A. Crook, J. Tuttle, L. J. Miller, and C. G. Wade, 1995: Initiation of deep convection along boundary layer convergence lines in a semitropical environment. *Mon. Wea. Rev.*, **123**, 291–313.
- Golding, B., 1998: Nimrod: A system for generating automatic very-short-range forecasts. *Meteor. Appl.*, **5**, 1–16.
- Gremillion, M. S., and R. E. Orville, 1999: Thunderstorm characteristics of cloud-to-ground lightning at the Kennedy Space Center, Florida: A study of lightning initiation signatures as indicated by WSR-88D. *Wea. Forecasting*, **14**, 640–649.
- Griffith, C. G., W. L. Woodley, P. G. Grube, D. W. Martin, J. Stout, and D. N. Sikdar, 1978: Rain estimation from geosynchronous satellite imagery—Visible and infrared studies. *Mon. Wea. Rev.*, **106**, 1153–1171.
- Hand, W. H., 1996: A technique for nowcasting heavy showers and thunderstorms. *Meteor. Appl.*, **3**, 31–41.
- , and B. J. Conway, 1995: An object-oriented approach to nowcasting showers. *Wea. Forecasting*, **10**, 327–341.
- Holle, R. L., and M. W. Maier, 1980: Tornado formation from downdraft interactions in the FACE mesonet. *Mon. Wea. Rev.*, **108**, 1010–1028.
- Johnson, D. B., P. Flament, and R. L. Bernstein, 1994: High-resolution satellite imagery for mesoscale meteorological studies. *Bull. Amer. Meteor. Soc.*, **75**, 5–33.
- Johnson, J. T., P. MacKeen, A. Witt, E. D. Mitchell, G. Stumpf, M. Eilt, and K. Thomas, 1998: The storm cell identification and tracking algorithm: An enhanced WSR-88D algorithm. *Wea. Forecasting*, **13**, 263–276.
- Kessinger, C. J., and C. K. Mueller, 1991: Background studies on nowcasting Florida thunderstorm activity in preparation for the CaPOW forecast experiment. Preprints, *25th Int. Conf. on Radar Meteorology*, Paris, France, Amer. Meteor. Soc., 416–419.
- Knight, C. A., and L. J. Miller, 1993: First radar echoes from cumulus clouds. *Bull. Amer. Meteor. Soc.*, **74**, 179–188.
- , W. D. Hall, and P. M. Roskowski, 1983: Visual cloud histories related to first radar echo formation in northeast Colorado cumulus. *J. Climate Appl. Meteor.*, **22**, 1022–1040.
- LeMone, M. A., 1973: The structure and dynamics of horizontal roll vortices in the planetary boundary layer. *J. Atmos. Sci.*, **30**, 1077–1091.
- Lovejoy, S., and G. L. Austin, 1979: The delineation of rain areas from visible and IR satellite data for GATE and mid-latitudes. *Atmos.–Ocean*, **17**, 77–92.
- McNeill, D., and P. Freiburger, 1993: *Fuzzy Logic: The Revolutionary Computer Technology that is Changing Our World*. Simon and Schuster, 319 pp.
- Menzel, W. P., and J. F. Purdom, 1994: Introducing GOES-I: The first of a new generation of geostationary operational environmental satellites. *Bull. Amer. Meteor. Soc.*, **75**, 757–781.
- Mueller, C. K., J. W. Wilson, and N. A. Crook, 1993: The utility of sounding and mesonet data to nowcast thunderstorm initiation. *Wea. Forecasting*, **8**, 132–146.
- , T. Saxen, R. Roberts, and J. W. Wilson, 2000: Evaluation of the NCAR thunderstorm Auto-Nowcast system. Preprints, *Ninth Conf. on Aviation, Range, and Aerospace Meteorology*, Orlando, FL, Amer. Meteor. Soc., 40–45.
- , —, —, —, T. Betancourt, S. Dettling, N. Oien, and J. Yee, 2003: NCAR Auto-Nowcast System. *Wea. Forecasting*, **18**, 545–561.
- Negri, A. J., and R. F. Adler, 1981: Relation of satellite-based thunderstorm intensity to radar-estimated rainfall. *J. Appl. Meteor.*, **20**, 288–300.
- OFCM, 1991: Doppler radar meteorological observations. Part A: System concepts, responsibilities and procedures. *Federal Meteorological Handbook*, No. 11, OFCM, Dept. of Commerce, 42 pp.
- Pielke, R., 1974: A three-dimensional numerical model of the sea breezes over south Florida. *Mon. Wea. Rev.*, **102**, 115–139.
- Pierce, C. E., P. J. Hardaker, C. G. Collier, and C. M. Haggett, 2000: GANDOLF: A system for generating automated nowcasts of convective precipitation. *Meteor. Appl.*, **7**, 341–360.
- Purdom, J. F. W., 1976: Some uses of high-resolution GOES imagery

- in the mesoscale forecasting of convection and its behavior. *Mon. Wea. Rev.*, **104**, 1474–1483.
- , and K. Marcus, 1982: Thunderstorm trigger mechanisms over the southeast United States. Preprints, *12th Conf. on Severe Local Storms*, San Antonio, TX, Amer. Meteor. Soc., 487–488.
- Rao, P. K., S. J. Holmes, R. J. Anderson, J. S. Winston, and P. E. Lehr, 1990: *Weather Satellites: Systems, Data, and Environmental Applications*. Amer. Meteor. Soc., 503 pp.
- Reynolds, D. W., and E. A. Smith, 1979: Detailed analysis of composited digital radar and satellite data. *Bull. Amer. Meteor. Soc.*, **60**, 1024–1037.
- Roberts, R. D., and J. W. Wilson, 1995: The genesis of three non-supercell tornadoes observed with dual-Doppler radar. *Mon. Wea. Rev.*, **123**, 3408–3438.
- , T. Saxen, C. Mueller, J. Wilson, A. Crook, J. Sun, and S. Henry, 1999: Operational application and use of NCAR's thunderstorm nowcasting system. Preprints, *Int. Conf. on Interactive Information and Processing Systems*, Dallas, TX, Amer. Meteor. Soc., 158–161.
- Saxen, T., C. Mueller, T. Jameson, and E. Hatfield, 1999: Determining key parameters for forecasting thunderstorms at White Sands Missile Range. Preprints, *29th Int. Conf. on Radar Meteorology*, Montreal, QC, Canada, Amer. Meteor. Soc., 9–12.
- Smith, S. B., J. T. Johnson, R. D. Roberts, S. M. Zubrick, and S. J. Weiss, 1998: The System for Convection Analysis and Nowcasting (SCAN): 1997–1998 field test. Preprints, *19th Conf. on Severe Local Storms*, Minneapolis, MN, Amer. Meteor. Soc., 790–793.
- Stensrud, D. J., and R. A. Maddox, 1988: Opposing mesoscale circulations: A case study. *Wea. Forecasting*, **3**, 189–204.
- Snyder, J. P., 1983: *Map Projections Used by the U.S. Geological Survey*. 2d ed. U.S. Government Printing Office, 313 pp.
- Szoke, E. J., M. L. Weisman, J. M. Brown, F. Caracena, and T. W. Schlatter, 1984: A subsynoptic analysis of the Denver tornadoes of 3 June 1981. *Mon. Wea. Rev.*, **112**, 790–808.
- Tag, P. M., R. L. Bankert, and L. R. Brody, 2000: An AVHRR multiple cloud-type classification package. *J. Appl. Meteor.*, **39**, 125–134.
- Tuttle, J. D., and G. B. Foote, 1990: Determination of the boundary layer airflow from a single Doppler radar. *J. Atmos. Oceanic Technol.*, **7**, 218–232.
- Wade, C. G., and G. B. Foote, 1982: The 22 July 1976 case study: Low-level outflow and mesoscale influences. *Hailstorms of the Central High Plains*, C. A. Knight and P. Squires, Eds., Vol. 2, Colorado Associated University Press, 115–130.
- Wakimoto, R. M., and N. T. Atkins, 1994: Observations of the sea-breeze front during CaPE. Part I: Single-Doppler, satellite, and cloud photogrammetry. *Mon. Wea. Rev.*, **122**, 1092–1114.
- , C. J. Kessinger, and D. E. Kingsmill, 1994: Kinematic, thermodynamic, and visual structure of low-reflectivity microbursts. *Mon. Wea. Rev.*, **122**, 72–92.
- Weckwerth, T. M., J. W. Wilson, and R. M. Wakimoto, 1996: Thermodynamic variability within the convective boundary layer due to horizontal convective rolls. *Mon. Wea. Rev.*, **124**, 769–784.
- , —, —, and N. A. Crook, 1997: Horizontal convective rolls: Determining the environmental conditions supporting their existence and characteristics. *Mon. Wea. Rev.*, **125**, 505–526.
- Weiss, C. E., 1978: Cloud location corrections near the horizon of an SMS image. Satellite Applications Information Note 78-8, Dept. of Commerce, Washington, DC, 8 pp.
- Wilson, J. W., and R. Carbone, 1984: Nowcasting with Doppler radar: The forecaster-computer relationship. *Nowcasting II*, K. Brown-ing, Ed., European Space Agency, 177–186.
- , and W. E. Schreiber, 1986: Initiation of convective storms at radar-observed boundary-layer convergence lines. *Mon. Wea. Rev.*, **114**, 2516–2536.
- , and C. K. Mueller, 1993: Nowcasts of thunderstorm initiation and evolution. *Wea. Forecasting*, **8**, 113–131.
- , G. B. Foote, N. A. Crook, J. C. Fankhauser, C. G. Wade, J. D. Tuttle, C. K. Mueller, and S. K. Krueger, 1992: The role of boundary-layer convergence zones and horizontal rolls in the initiation of thunderstorms: A case study. *Mon. Wea. Rev.*, **120**, 1785–1815.
- , T. M. Weckwerth, J. Vivekanandan, R. M. Wakimoto, and R. W. Russell, 1994: Boundary layer clear-air radar echoes: Origin of echoes and accuracy of derived winds. *J. Atmos. Oceanic Technol.*, **11**, 1184–1206.